Thin film magnetostrictive sensor with on-chip readout

by

Yong Lu

A thesis
presented to the University of Waterloo
in fulfilment of the
thesis requirement for the degree of
Doctor of Philosophy
in
Electrical Engineering

Waterloo, Ontario, Canada, 1997

©Yong Lu 1997

National Library of Canada
Acquisitions and Bibliographic Services
395 Wellington Street
Ottawa ON K1A 0N4
Canada

Bibliothèque nationale du Canada
Acquisitions et services bibliographiques
395, rue Wellington
Ottawa ON K1A 0N4
Canada

Your file Votre référence

Our file Notre référence

The author has granted a non-exclusive licence allowing the National Library of Canada to reproduce, loan, distribute or sell copies of this thesis in microform, paper or electronic formats.

The author retains ownership of the copyright in this thesis. Neither the thesis nor substantial extracts from it may be printed or otherwise reproduced without the author's permission.

L'auteur a accordé une licence non exclusive permettant à la Bibliothèque nationale du Canada de reproduire, prêter, distribuer ou vendre des copies de cette thèse sous la forme de microfiche/film, de reproduction sur papier ou sur format électronique.

L'auteur conserve la propriété du droit d'auteur qui protège cette thèse. Ni la thèse ni des extraits substantiels de celle-ci ne doivent être imprimés ou autrement reproduits sans son autorisation.

0-612-22216-0

Canada

The University of Waterloo requires the signatures of all persons using or photocopying this thesis. Please sign below, and give address and date.

Acknowledgements

I would like to express my gratitude to my supervisor Professor A. Nathan for his guidance, support, and the numerous stimulating discussions. His help and optimism made this research pleasurable.

Special thanks go to Mr. R. Grant for suggestions on upgrading the deposition system and for discussions related to process and fabrication issues. My thanks also go to Dr. Y. Bhatnagar and Mr. D. Kwasnicki for providing required training in the Lab.

My appreciation to Professor V. Karanassios for providing the ICP analysis, Dr. Y. B. Ning of Alberta Microelectronic Center for assistance with the low stress nitride deposition and Mr. W. H. Gong of McMaster University for the X-ray material characterizations.

My thanks to Professor W. Huang for unlimited access to his measurement laboratory and Mr. E. Praetzel for assistance with fibre optical measurements.

I would like to thank all my colleagues, in particular Dr. K. Benaissa, Mr. Q. Ma and Dr. F. Chen for many inspiring discussions.

I am honored to have Dr. D. Tang of IBM Almaden Research Laboratory as my external examiner, and my thanks to the members of my Ph.D examination committee.

Finally, with all my heart, I would like to thank my wife, Xiaohong Qiu, for her patience, sacrifice and encouragement throughout this work; to my parents and sisters for their moral support.

Abstract

We report the first successful integration of magnetostrictive Metglas2605S2 ($Fe_{78}Si_9B_{13}$) thin film sensor system on silicon with high resolution capacitive readout. A deposition process for Metglas thin film has been developed to allow easy control of thin film composition. An amorphous microstructure has been achieved over a wide temperature range, and in-situ magnetic domain alignment can be accomplished at room temperature as the film is deposited. The thin film has been characterized by Inductively Coupled Plasma (ICP) analysis for composition, X-Ray Diffraction (XRD) spectrum for microstructure, magnetization measurement for domain alignment and capacitive measurement for magnetostriction. The thin film is suitable for any magnetostrictive sensor applications, in particular, for IC compatible microsensors and microactuators. We have demonstrated the subsequent process integration with IC fabrication technology. Here, the Metglas thin film has been successfully incorporated to micromechanical structures using surface micromachining with appropriate choice of sacrificial layer and low stress mechanical layers.

In addition, we present the development of a high resolution capacitive readout circuit co-integrated with the sensor. The readout circuit is based on a floating gate MOSFET configuration, requiring just a single transistor and operated at DC or low frequencies. Using the prototype developed in-house, we have successfully demonstrated a resolution capability of 10^{-17} F, this translates to a few $\AA$ in terms of cantilever beam deflection of the sensor. The floating gate readout technique is readily applicable to any capacitive sensors with a need for on-chip readout. It is also an ideal in-situ test structure for on IC chip process characterization and parameter extraction.

Contents

1 Introduction **1**

1.1 Motivation 1

1.2 Magnetostrictive sensors 3

1.3 Problem statement 4

1.4 Thesis structure 5

2 Metglas ribbon sensors **7**

2.1 Materials 8

2.2 Magnetomechanical coupling 14

2.3 Signal processing 16

3 Metglas thin film deposition and characterization **21**

3.1 Basic requirements 21

3.2 Deposition system and deposition conditions 22

3.3 Microstructures 24

3.4 In-situ magnetization 26

3.5 Magnetic characterization 28

4 Metglas thin film sensor and readout circuit 35

4.1 Design considerations 37

4.1.1 Mechanical consideration 37

4.1.2 Electrical consideration 38

4.2 Sensor fabrication 39

4.3 Sensor readout circuit 41

4.3.1 DC characteristics 45

4.3.2 DC effects due to Miller capacitance 46

4.3.3 Analysis of the circuit gain 48

4.4 Magnetic field measurement results 53

4.5 Discussion 54

4.5.1 Gain enhancement using advanced MOSFET 54

4.5.2 Non-magnetic packaging 57

4.5.3 Other applications of the floating gate readout circuit 57

5 Conclusions and outlook 59

5.1 Summary of contributions 59

5.2 Future perspective 60

A Fabrication sequence of integrated Metglas thin film sensor 63

A.1 Mask making 63

A.2 IC and sensor fabrication details 67

B Ferromagnetism, Magnetic domain and magnetostriction **70**

B.1 Ferromagnetism and Curie temperature 71

B.2 Magnetic anisotropy 73

B.3 Magnetic domains 76

B.4 Magnetization process 78

B.5 Magnetostriction 80

B.6 Effect of stress and loading 84

C Metglas thin film fibre-optic interferometer **86**

D Analytic expression of small signal voltage gain **90**

Bibliography **92**

List of Tables

1.1 Comparison of different magnetometers. For reference, the earth's field is about 0.5 Oe. 2

3.1 Deposition parameters. 24

3.2 Young's moduli and Poisson ratios for Metglas thin film and glass substrate. 32

4.1 MOSFET parameters and parasitic capacitances. 48

A.1 Process steps in Fig.4.2 (a). 67

A.2 Process steps in Fig.4.2 (b) - (e). 68

A.3 Typical process conditions used in this thesis. 69

C.1 Specifications of fibre and couplers used for Metglas thin film fibre-optic interferometer. 87

List of Figures

1.1 Magnetostrictive sensor based on optical fiber interferometer 3

2.1 Material choice for magnetic transducers. 9

2.2 (a) field annealing, (b) stress-annealing, (C) surface crystallization. 13

2.3 Epoxy induced stress. 15

2.4 AC signal detection in an optical interferometer. 17

2.5 The dynamic responsivity of magnetostrictive materials. 19

3.1 Sputtering deposition system. 23

3.2 X-ray diffraction pattern of samples deposited at room temperature (X1), 300°C (X2) and 400°C (X3). X1 has been vacuum annealed at 500°C for one hour. 25

3.3 Magnetizing the thin film during deposition. 27

3.4 Measurement arrangement for characterization of the thin film B-H curve. 29

3.5 Experimentally measured dB/dt vs H curve of the as-deposited Metglas2605S2 thin film and the corresponding B-H curve obtained by numerical integration. 30

3.6 Capacitive measurement setup for thin film magnetostriction characterization. 31

3.7 Measurement result of magnetostriction on Metglas thin film. . . . 33

4.1 Operation principle of the IC compatible Metglas thin film sensor. . 36

4.2 (a) poly fixed plate connected to the amplifier, (b) Metglas top layer connected to the amplifier. 38

4.3 The fabrication process of MOSFET and sensor 40

4.4 SEM of suspended cantilever beam with Metglas film (400 x 100 x 2 μm). 42

4.5 Photograph of Metglas thin film sensor with readout circuit. 43

4.6 Floating gate configuration. 44

4.7 Current-voltage characteristics of the readout MOSFET without sensor. 45

4.8 Current-voltage characteristics of the (sensor) charge coupled floating gate readout circuit. 46

4.9 (a) Parasitic capacitances associated with MOSFET (b) DC equivalent circuit. 47

4.10 (a) Floating gate amplifier. (b) Converting ΔC_x to v_s at the input. 49

4.11 The dependence of gate voltage and AC gain on Miller capacitance. 52

4.12 The applied field (H) and the output response for an AC magnetic field at 500 Hz, the output shown is obtained with an off-chip load of 7.5 kΩ. 53

4.13 Strain induced in Metglas thin film as a function of the magnetic field H (1 Oe = 1 Gauss in vacuum). Small AC fields can be measured with a DC field bias. 55

A.1 Mask making flow. 63

A.2 Overview of the mask set. 64

A.3 Windows for gate oxide. 65

A.4 Gate and sensor capacitor poly. 65

A.5 Contact holes. 65

A.6 Metal contact and sacrificial layer. 65

A.7 Windows on passivation nitride for metal pads and sacrificial layer. 66

A.8 Metglas pattern. 66

A.9 Etching windows for sacrificial layer. 66

B.1 The magnetization curve of Fe [43], Ni [44] and Co [45]. 74

B.2 The origin of magnetic domains. 78

B.3 Typical magnetization curve, showing the dominant magnetization processes in the different regions of the curve. 79

B.4 The magnetostriction process. 82

C.1 Thin film deposition setup for optical fibres. 87

C.2 Metglas coated fibre optic interferometer. 88

C.3 Response of the Metglas coated fibre optic interferometer to a driving field of 60 Oe at 500 Hz. 89

Chapter 1

Introduction

1.1 Motivation

Over the past three decades, significant progress has been made on the storage, processing and transmission of information, with the development of sophisticated microelectronics and powerful computer systems. Nowadays, there is growing demand on smart chips that gather information from the non-electrical world, process the information using electronic infrastructure, and subsequently output the information in the form of electrical or non-electrical actions. The success of such chips depends largely on the development of microsensors and microactuators [1, 2].

Sensors and actuators have been with us since ancient time. For example, the magnetic compass made of magnetite (Fe_3O_4) was known to man for at least two thousand years. Because of their importance to our well being, the search for sensors that have high sensitivity, good linearity and large dynamic range has always been actively pursued by mankind. Traditionally, sensors are designed to fulfill a

certain functionality. They were often large in size and with non-electrical output, hence not compatible with the modern microelectronic technologies. However, they provided very important knowledge base for developing the state-of-the-art microsensors. Examples of magnetic sensors are listed in Table 1.1 [3].

Magnetic sensors	Detectable range (Oe)
SQUID Magnetometer	$10^{-10} - 10^{-4}$
Fiber-Optic Magnetostrictive Magnetometer	$10^{-7} - 10$
Inductive Coil Magnetometer	$10^{-6} - -$
Flux Gate Magnetometer	$10^{-6} - 100$
Magnetoresistive Magnetometer	$10^{-2} - 50$
Magnetotransistor	$10^{-5} -$
Hall Magnetometer	$10^{-3} - 1000$

Table 1.1: Comparison of different magnetometers. For reference, the earth's field is about 0.5 Oe.

The current work is inspired by what has been achieved with the fibre-optic magnetostrictive magnetometer. Our goal is to develop a microsensor system on silicon which takes the advantage of both the high sensitivity of magnetostrictive magnetometers and the signal processing capability of microelectronics.

1.2 Magnetostrictive sensors

Magnetostriction is a phenomenon exhibited by most of the ferromagnetic materials. It describes the change in linear dimension of the material in the presence of a magnetic field. In general, the larger the magnetostriction, the harder it is for the material to be magnetized. In most applications, magnetostriction is a negative factor since it is responsible for stress, loss, magnetic anisotropy and low permeability. In recent years, extensive research efforts devoted to amorphous magnetic materials have brought about some breakthroughs. For example, a family of Fe-based amorphous alloys called Metglas has been found to possess both large magnetostriction and low saturation field [4].

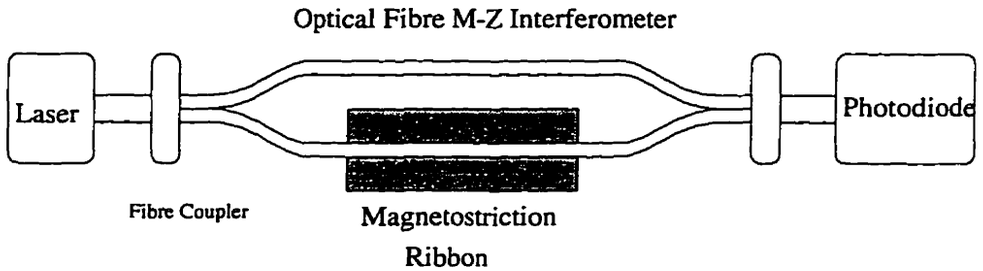


Figure 1.1: Magnetostrictive sensor based on optical fiber interferometer

This unique material property has recently drawn significant interest in sensor and actuator applications. In magnetostrictive sensors, the magnetic field is first converted to a mechanical strain in the Metglas ribbon, which is subsequently measured by a mechanical transducer. Laboratory prototypes have been fabricated utilize fibre optic interferometers [5] (see Fig.1.1) or piezoelectric polymers [6] as the mechanical transducer. Exciting results have been reported, which demonstrate a

magnetic field resolution of 10^{-6} Oe. Although the magnetostrictive magnetometer is not as sensitive as the SQUID, it does not require cryogenic cooling and its sensitivity and noise behavior is comparable to, or better than, the more conventional induction coil and flux gate magnetometer, which are bulkier and more expensive. When fully developed, the magnetostrictive magnetometer will potentially replace the induction coil and flux gate magnetometer in applications such as navigation (magnetic compass) and mineral prospecting.

1.3 Problem statement

Although the results of previous work look promising, there are several problems generally acknowledged. Firstly, the commercially available as-cast Metglas ribbon does not readily lend itself to sensor applications due to the high internal stress and random magnetic domain structure. In order to reduce the stress and to align the domains, a high temperature (around 400°C) post annealing is needed in the presence of a magnetizing field. During the annealing procedure, ribbons need to be protected by vacuum or inert gas to prevent oxidation. Secondly, the size of current prototypes, ranging from 3 cm to more than 30 cm, is too large for microtransducer applications and cannot be integrated with circuitry on silicon for realization of smart sensor systems. More importantly, there are no adequate means of coupling the magnetic strain induced in the Metglas material to the mechanical transducer. Currently, Metglas ribbons are glued onto optical fibres or piezoelectric polymers by epoxy. The epoxy layer not only increases the mechanical loading of the ribbon, which reduces the actual strain coupled, but also disturbs the magnetic domain structure optimized previously by annealing, by virtue of interface stresses induced

during the curing process of the epoxy [7].

These issues are obstacles for this otherwise very attractive technology. Aiming to solve these problems, we have made progress in the following three areas. First, the Metglas ribbon is replaced by a Metglas thin film deposited by DC magnetron sputtering [8]. The film is domain aligned in the predesigned direction, and has low interface stresses with the substrate. Second, Metglas thin film sensors have been realized on silicon with a standard IC technology. Third, a MOSFET circuit has been successfully integrated with the sensor on silicon, resolving the key challenge of small capacitive signal readout [9].

1.4 Thesis structure

We review the previous work based on Metglas ribbon and fibre optical interferometers in chapter 2 and establish necessary technical background for later chapters.

Chapter 3 discusses the deposition and characterization of the Metglas thin film. Characterization techniques include Inductively Coupled Plasma analysis (ICP) for stoichiometry, X-Ray Diffraction spectrum (XRD) for microstructure, thin film magnetization curve measurement for easy axis identification and magnetostriction measurements for magnetoelastic properties. Emphasis will be given to the in-situ magnetic domain alignment, stress reduction at the interface and IC compatibility.

Chapter 4 describes the realization of the magnetostrictive microsensor system

on silicon using the standard MOSFET process and surface micromachining technology. We will analyse the design, characterization and optimization issues of the floating gate MOSFET readout circuit to achieve an attoFarad capacitive resolution. A brief discussion is also given on the application potential of the floating gate MOSFET readout circuit to other areas, notably in IC process parameter extraction and chemical sensing.

Chapter 5 summarizes the major achievements of the current work, and provides the possible directions for further improvement.

Chapter 2

Metglas ribbon sensors

The development of magnetostrictive magnetometers dated back to the early 80's, following progress in two key areas: commercial availability of Metglas ribbons that possess large magnetostriction and low saturation field and applications of the fibre optical interferometer as high sensitivity strain gauge.

The use of an optical fibre interferometer with magnetostrictive material, for magnetic field measurement was first proposed by A.Yariv and H.Winsor in 1980 [10]. They suggested the use of a very long sensing arm (kilometers) to accumulate the tiny strain in the magnetostrictive material to yield a length change comparable to that of the optical wavelength. By comparing the phase of the sensing and the reference arms (see Fig.1.1), the magnetic field strength is retrived from the measurement of optical intensity at the interferometer output. At about the same time, D.A Jackson [11] *et al.* demonstrated that the fibre-optic interferometer has an extremely good resolution on length ($10^{-3}\mathring{A}$!), so that the long sensing arm suggested by Yariv is not actually needed.

From the mid 80's to early 90's, there has been extensive research on magnetostrictive materials. Different material compositions and annealing conditions have been studied to optimize their magnetic properties. It turns out that one of the major challenges comes from efficient coupling of the magnetic field induced strain to the optical fibre.

In the following sections, we will review the progress on magnetostrictive materials, high sensitivity fibre optic strain gauges, low noise signal readout and issues related to magnetic - mechanical coupling. Our discussion will be kept simple; a more in-depth description can be found the the appendix B.

2.1 Materials

Magnetostrictive materials are characterized by two key parameters: saturation magnetostrictive strain, λ_s and saturation magnetic field, H_s. The former is a measure of the size of the effect, while the latter indicates how easy to achieve it. Since the magnetostrictive transducer is a device that converts energy from a magnetic domain to a mechanical domain, a large λ_s and small H_s are desirable for high transduction efficiency.

Two kinds of materials are important for magnetic transducers. The first is the so called "giant" magnetostrictive material made of the alloy of rare earth element (e.g., Tb, Dy, Sm, Ho) and transition elements (Fe, Ni, Co). They possess the high-

est known saturation strain (λ_s= 1759 ppm for $TbFe_2$) at room temperature, but require a very high field (> 1000 Oe) to operate [12]. These materials are candidates for magnetic actuators. A wireless mobile micro robot has been demonstrated using giant magnetostrictive alloy [13]. The second class of magnetostrictive material is the iron based amorphous alloys often referred to as Metglas. These materials have a combination of large λ_s (20-60 ppm) and low saturation field (< 1 Oe) [14]. It is the low saturation field that makes these materials particularly attractive for sensor applications.

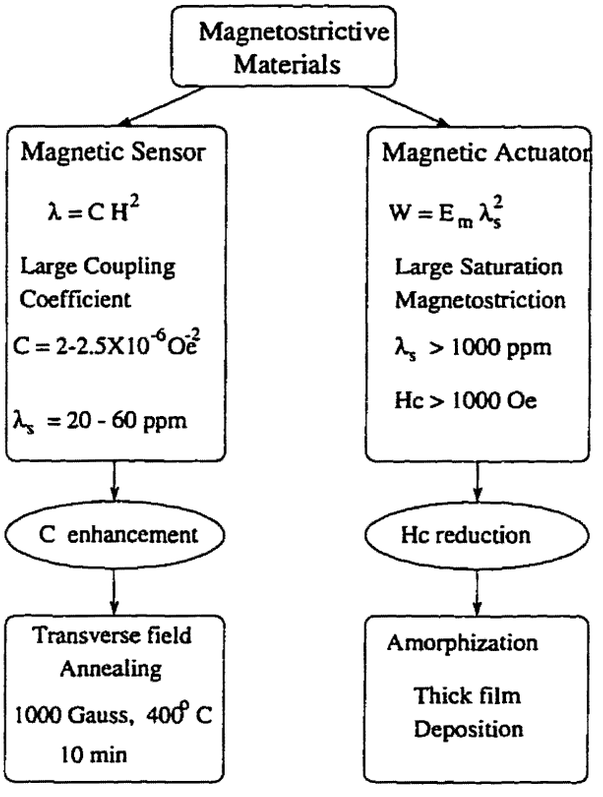


Figure 2.1: Material choice for magnetic transducers.

Figure 2.1 highlights the main difference between these two groups of materials and associated processes needed to improve their performance. Although both materials are technically important, our attention will focus on Metglas since our main interest is in sensor applications. It is important to recognize here the unique properties of magnetostrictive materials.

It is well known that λ_s and H_s are not just material related quantities, they are very much influenced by the history of mechanical, thermal, and magnetic treatments [15]. In general, stress increases H_s (or hardens the material), while annealing helps release the stress (or softens the material). If a magnetic field is applied during the annealing process, domains will rotate towards the direction of the field. This domain aligned state may remain in magnetostrictive materials if the temperature is withdrawn before the field. Because magnetostriction is the result of domain rotation, it depends very much on the original magnetic domain structure. Since amorphous materials do not possess a lattice structure, they can be regarded as isotropic. The magnetostriction in such materials can be well described by a simple model proposed by Livingston [16]:

(1) In isotropic materials (polycrystalline or amorphous) under nonsaturated conditions, λ depends on both the value of saturation magnetostriction λ_s (a material constant) and on the change of magnetic domain configuration from its initial arrangement [17, 18]:

$$\lambda = \frac{3}{2}\lambda_s(< cos^2\theta > - < cos^2\theta >_o) \tag{2.1}$$

Here, θ is the angle between local magnetization of the domain and the external

magnetic field, $< cos^2\theta >$ refers to the average value of magnetic moment distribution in the field (which equates to unity when $H > H_s$), and $< cos^2\theta >_o$ is the average value of the original state. Clearly, λ lies somewhere between zero and $\frac{3}{2}\lambda_s$, depending on the original configuration of the domain structure, and has a maximum value when $< cos^2\theta >_o = 0$, *i.e.*, when all of the domains are initially aligned perpendicular to the field. Any spread in the direction of initial moments (say the moments lie within a fan or cone of $90° \pm \delta$) will reduce the maximum possible value of λ. This reduced saturation strain is sometimes also referred to as *engineering magnetostriction* λ_e. In practice, λ_e is more important since it determines the maximum response of the material.

(2) In metallic glasses, the 90° state can be achieved by annealing the sample in the presence of a transverse magnetic field, which defines the direction of the macroscopic easy axis. Since the amorphous material does not have any macroscopic order, a uniaxial anisotropy can be developed along the direction of the annealing field. In sensing applications, an external magnetic field perpendicular to the easy axis has the characteristic of driving magnetic moments away from this axis, causing an energy increase of $K_u cos^2\theta$. Here, K_u is the anisotropic energy. At low fields, λ can be related to the external magnetic field **H** through the following simple equation:

$$\lambda = CH^2 \tag{2.2}$$

where

$$C = \frac{3}{2}\frac{\lambda_s}{H_a^2} \tag{2.3}$$

and $H_a \equiv 2K_u/M_s$ is the anisotropic field associated with the easy axis. This is equivalent to H_s in metallic glasses. When the ideal conditions are not completely satisfied (*i.e.*, $\delta \neq 0$ or a residual stress exists), equation 2.2 still holds approximately, but C reduces to a smaller value, C_{eff}. The figure of merit for sensor applications is this effective magnetomechanical coupling (or piezomagnetic) coefficient C_{eff}. It is clear that a large C_{eff} requires a combination of large λ_s and small H_a.

Since the mid 80's, there are several groups working actively on metallic glass materials for sensor applications. These include the Naval Research Lab. [19, 20] in the US, University of Bath [21], University of Kent [5] and GEC Research Lab. [7] in the UK. Most of the research work is focused on iron based amorphous alloy families called Metglas, in particular, Metglas2605S2 ($Fe_{78}Si_9B_{13}$) and Metglas2605SC ($Fe_{81}B_{13.5}Si_{3.5}C_2$). These are all commercially available in the form of a thin ribbon(15-50 μm) with saturation magnetostriction λ_s of approximately $+30 \times 10^{-6}$ [19]. One of the most important factors affecting the performance of Metglas ribbon is the magnetic domain orientation. Several approaches can be applied to control the domain alignment.

Bucholtz *et al.* [19, 20] have studied the effect of field annealing (Fig.2.2 (a)) at various temperatures, annealing times, and field strengths. They find that the spread of initial magnetic moment orientation δ can be controlled to within a few degrees by annealing the ribbons in a field directed along the width of the sample. The effective coupling constant C_{eff} can be improved by a factor of 10 compared to the as-cast material, with a maximum observed value of $(2.0 - 2.5) \times 10^{-6}$ Oe^{-2}. H_a is found to be 0.81 Oe for Metglas2605S2 and 0.9 Oe for Metglas2605SC. The

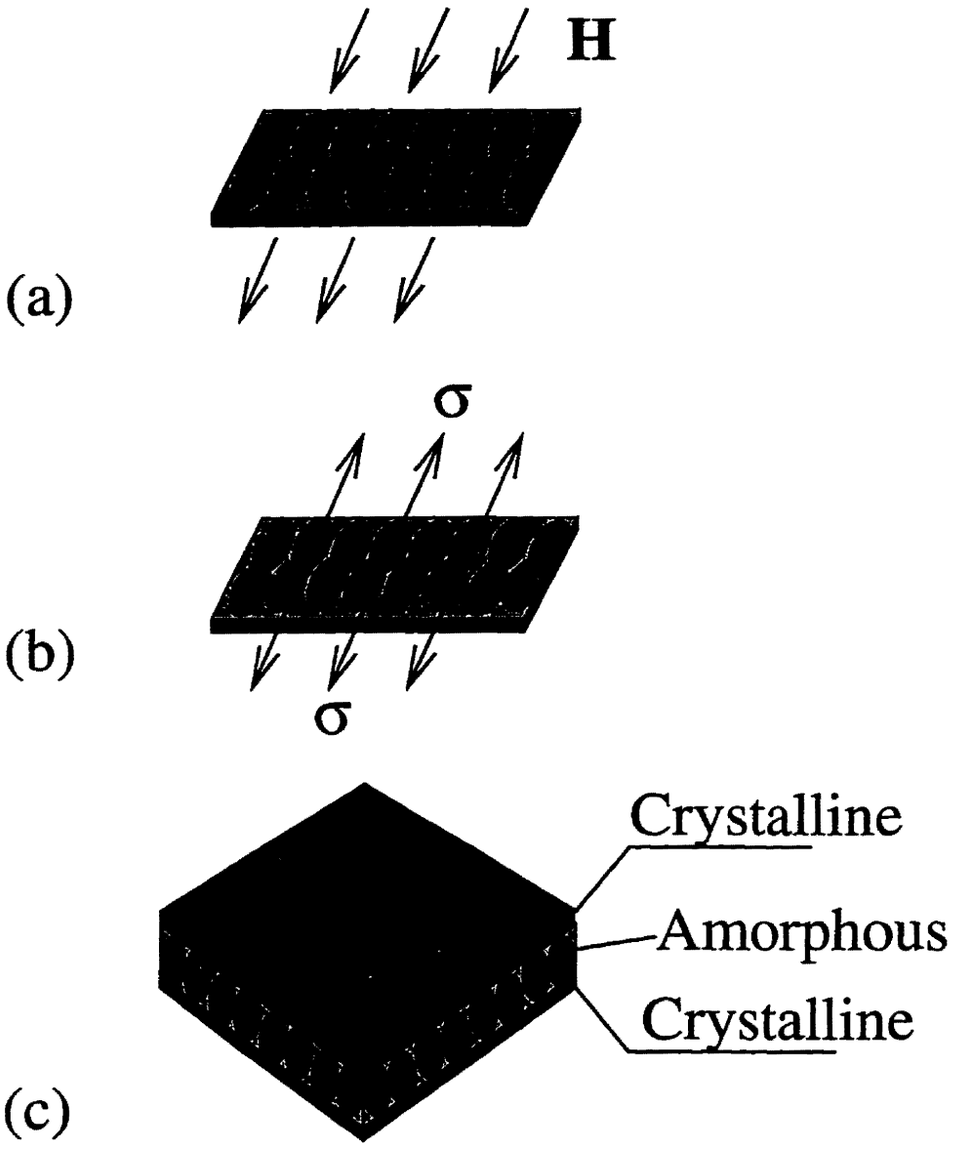


Figure 2.2: (a) field annealing, (b) stress-annealing, (C) surface crystallization.

best result is obtained under an annealing field of 1200 Oe at 400°C for 3600 sec.

Kraus *et al.* [22] studied changes of domain structure in stress-annealing (Fig.2.2 (b)). Stress affects the magnetic domain structures through magnetomechanical coupling. They observed that an uniaxial tension can rotate the domains towards the stress axis (for positive magnetostriction material), making it easier to magnetize along the direction. This is however a reversible process, since domains return to their original orientation upon withdrawal of the stress. To keep the aligned domain structure permanent, a temperature of 200°C is needed while the stress is applied.

Surface crystallization [7] is a special case of stress-annealing (Fig.2.2 (c)). Samples were heated up to 450°C, to allow a slight crystallization at the surface of the ribbon. Because the density of the crystals is about 2-3% higher than that of the amorphous phase, the surface layer will contract. This imposes a biaxial compression on the amorphous layer sandwiched in the center, pushing the domains to orient in the direction perpendicular to the ribbon surface.

2.2 Magnetomechanical coupling

Magnetostrictive sensors are tandem transducers which involve at least a two stage transduction process. The mechanical strain generated by magnetostriction needs to be coupled to a secondary transducer such as a fibre-optic interferometer [5], cantilever-capacitor [24], or a piezoelectric element [6], through a proper coupling.

In early work, the transverse-field-annealed metallic glass ribbon was simply glued onto the subsequent transducer stage by epoxy. It was soon realized that the epoxy had a great negative impact on the performance of the magnetometer. Bucholtz *et al.* [27] showed that the epoxy could reduce the magnetic strain by a factor of 6. The main cause for such a degradation was believed to be the stress-induced easy axis reorientation. As the epoxy cured, it placed a biaxial compressive stress on the ribbon which pulled the easy axis away from the ideal orientation (Fig.2.3). Mermelstein [28] further pointed out that stress was also a source of noise. One way around this was to use a lower modulus adhesive [27] or even a viscous fluid [29] as the bonding medium. Amongst other difficulties, however, this technique compromises the low frequency behavior of the device, and thus it is not a suitable solution.

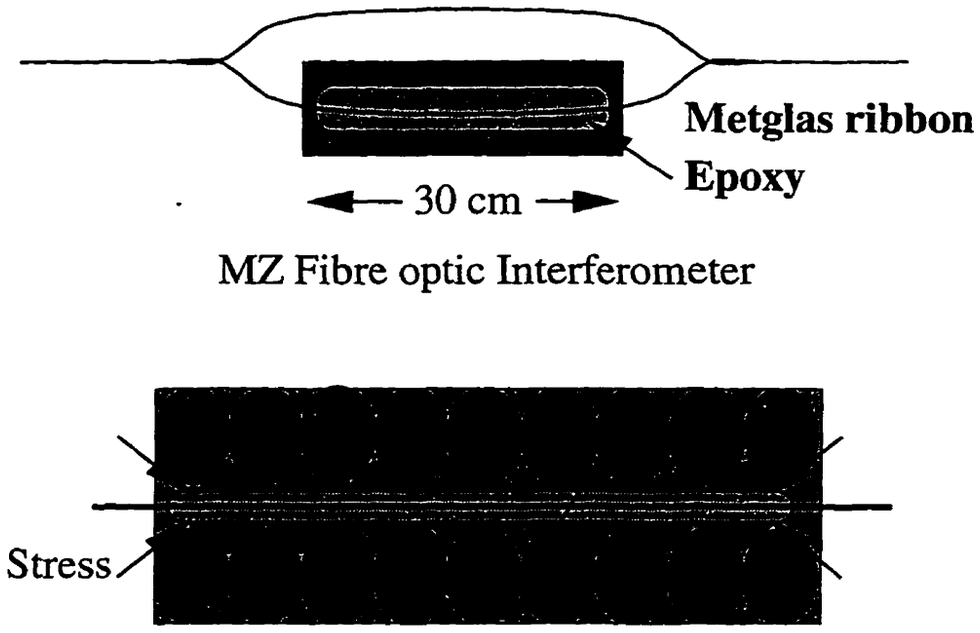


Figure 2.3: Epoxy induced stress.

Vincent *et al.* [7] suggested the use of a surface crystallized ribbon as the magnetostrictive material. As discussed in section 2.1, the surface crystallized ribbon has an easy axis oriented perpendicular to its surface, the compressive stress associated with epoxy cannot disturb the orientation of the moments, hence has less negative impact on the overall performance of the sensor. Although it overcomes the problem of domain re-orientation, this method has its own shortcomings. As the authors [7] point out, surface crystallization tends to make the ribbon brittle which presents handling problems during assembly.

2.3 Signal processing

Sensors are generally characterized by two parameters: sensitivity and resolution. The former is the system response to the measurand while the latter is the minimum detectable signal level, which can be improved by either increasing the output (higher sensitivity) or reducing the noise [30].

For a tandem sensor system like the magnetostrictive magnetometer, the overall sensitivity is the product of the sensitivities at each transduction stage. In order to achieve a good performance, every stage needs to be optimized. The sensitivity of the first stage is determined by the material properties as discussed in section 2.1. The sensitivity of the second stage depends on the individual system chosen. With the fibre optic interferometer as an example, the sensitivity is proportional to the length of its sensing arm. Theoretically, this can be improved by simply increasing the length of the sensing arm. In practice, however, a very long sensing arm, as suggested by Yariv *et al.*, has never been implemented. Apart from the fact that

a large size is inconvenient for many applications, it also limits the spatial resolution of the device. Furthermore, a larger device is more vulnerable to temperature fluctuations, vibration, and frequency drifts of the laser source. In addition, when the two arms are out of balance, which is more likely for longer arms, the sensor system constantly drifts, and hence does not function as desired. This implies that an increase in sensitivity may not necessarily be beneficial to the resolution [30]. This is also true for other kinds of strain-sensitive transducers.

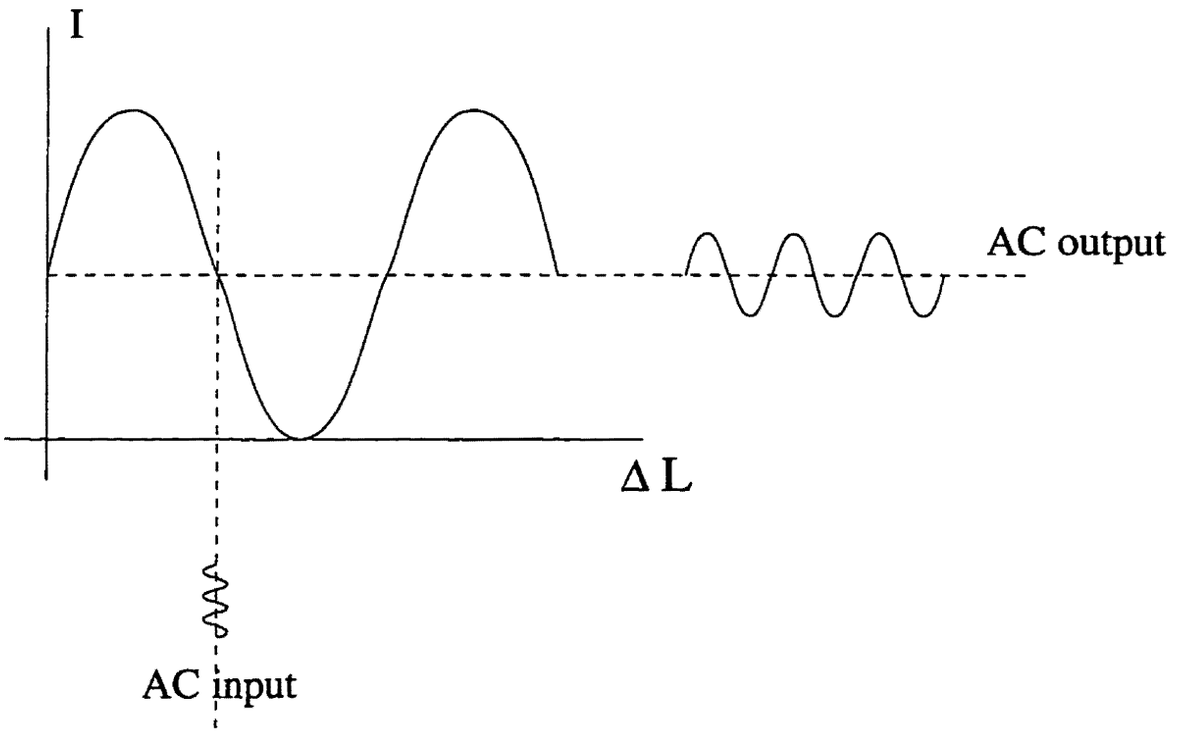


Figure 2.4: AC signal detection in an optical interferometer.

Thus limiting the size of the device, for reasons explained earlier, suggests that resolution improvement is determined by reduction of the noise level. Actually, the

subatomic resolution of interferometers mentioned previously can never be achieved by directly exposing the magnetometer to the slowly varying field that is to be measured. Here, the optical interferometer is not capable of distinguishing the magnetically-induced signal phase shift from environmentally induced noise and drift, which are known to predominate at low frequencies ($f < 10$ Hz). To exploit the high resolution potential of the optical interferometer, the DC or low frequency signal has to be modulated as a high frequency AC displacement (Fig.2.4).

The low frequency signal modulation in magnetostrictive materials is made possible by its nonlinearity, *i.e.*, the magnetic strain is a nonlinear function of magnetic field, $\lambda = CH^2$. When driven by an AC field H_{ac}, the total magnetic field **H** experienced by the magnetometer is,

$$H = H_{dc} + H_{ac} sin\omega t \tag{2.4}$$

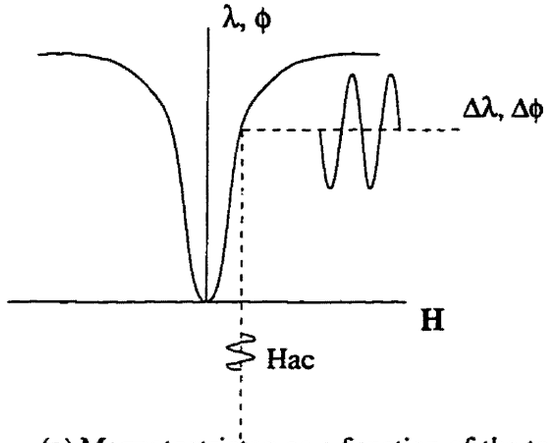
and the mechanical strain becomes:

$$\lambda = CH^2 = C[H_{dc}^2 + 2H_{dc}H_{ac}sin\omega t + H_{ac}^2 sin^2\omega t] = \lambda_{dc} + \lambda_\omega sin\omega t + \lambda_{2\omega} cos2\omega t \tag{2.5}$$

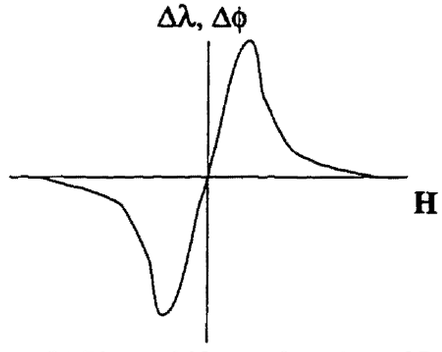
Among the three terms, the first harmonic term $\lambda_\omega = 2CH_{dc}H_{ac}$ is of particular interest. Here the DC signal, H_{dc} has become part of the high frequency ($\omega \sim$ kHz) AC amplitude, or the high frequency signal. What seems more interesting is the fact that the magnetostrictive material functions not only as a mixer (by making use of H_{ac} as carrier of the H_{dc}) to take full advantage of the high resolution at high frequency, but also as an amplifier when $H_{dc} < H_{ac}$. The amplification ratio β can be expressed as:

$$\beta = \frac{\lambda_\omega}{\lambda(H_{ac}=0)} = \frac{2CH_{dc}H_{ac}}{CH_{dc}^2} = 2\frac{H_{ac}}{H_{dc}} \tag{2.6}$$

If $H_{ac} = 1$ Oe, and for a DC signal of $H_{dc} = 10^{-5}$ Oe, β can be as large as 2×10^5. This is one of the reasons why magnetostrictive sensors can have very high sensitivity.



(a) Magnetostricton as a function of the total field.



(b) Phase shift as a function of DC field
in the presence of an AC driving field.

Figure 2.5: The dynamic responsivity of magnetostrictive materials.

Figure 2.5 (a) represents the response of the strain to the total magnetic field, and Fig. 2.5 (b) is the derivative of the curve shown in (a). For a fixed driving field H_{ac}, the DC signal can be represented by Fig. 2.5 (b). Within the dynamic range, the dynamic responsivity is fairly linear with H_{dc}. Actually, the signal modulation process is analogous to AM radio broadcasting; audio signals are sent as the amplitude envelop of a high frequency radio wave with noise being much smaller than the audio level.

In summary, good magnetostrictive materials (Metglas) are commercially available. Various schemes of obtaining a optimal domain structure have been studied, including field annealing, stress annealing and partial surface crystalization. However, what remains to be solved is the issue of efficient mechanical coupling between the Metglas and the strain sensor without disturbing the magnetic domain structure in the former. In addition, the issue of developing a process that is compatible with the IC technology should be addressed. These constitute the topics of the next chapter.

Chapter 3

Metglas thin film deposition and characterization

3.1 Basic requirements

In the development of magnetostrictive sensors, Metglas thin film has not received as much attention as it deserves. This may be partly attributed to the ease of availability of high quality ribbons. Although good performance prototypes can be demonstrated with the ribbon, the problems associated with epoxy bonding make the technology poor in reproducibility and high in assembly cost, hence making it difficult for high volume production [7]. The problem is not due to the Metglas ribbon nor the fibre optical interferometer, but due to the incompatibility of the two technologies. Eliminating the epoxy layer using thin film deposition appears to be a natural solution.

To achieve a device quality Metglas thin film, three requirements have to be

satisfied, namely, the right alloy composition, the correct microstructure (amorphous), and fully aligned magnetic domains in the desired direction. In addition, the deposition has to be carried out at room temperature if the thermal expansion related interface stress is to be eliminated. Besides solving the mechanical coupling problem, the thin film technology has to be incorporated with the IC process, to make possible the integration of the sensor and the readout circuit on the same chip.

Metglas2605S2 ($Fe_{78}Si_9B_{13}$) has been chosen for the current study because of its superior magnetic properties and relatively simple chemical composition among the Metglas family. We use DC magnetron sputtering as the deposition method because of its ease of composition control [31, 32]. The major advantage of sputtering over other deposition techniques is that it can transfer the stoichiometry of an alloy target to the substrate as long as the target is made of non-volatile elements, and no direct high energy particle bombardment (or reverse sputtering) occurs at the substrate. Hence the alloy composition of the thin film can be controlled simply by choosing the right composition for the target.

3.2 Deposition system and deposition conditions

The sputtering system for Metglas thin film was developed by upgrading an old evaporation station. The vacuum is provided by a standard mechanical-diffusion pump system. A base pressure of low 10^{-6} torr is achieved with the help of a liquid nitrogen trap. A special sputtering gun arrangement has been employed to allow penetration of the magnetic field from the gun through the 0.125 inch thick

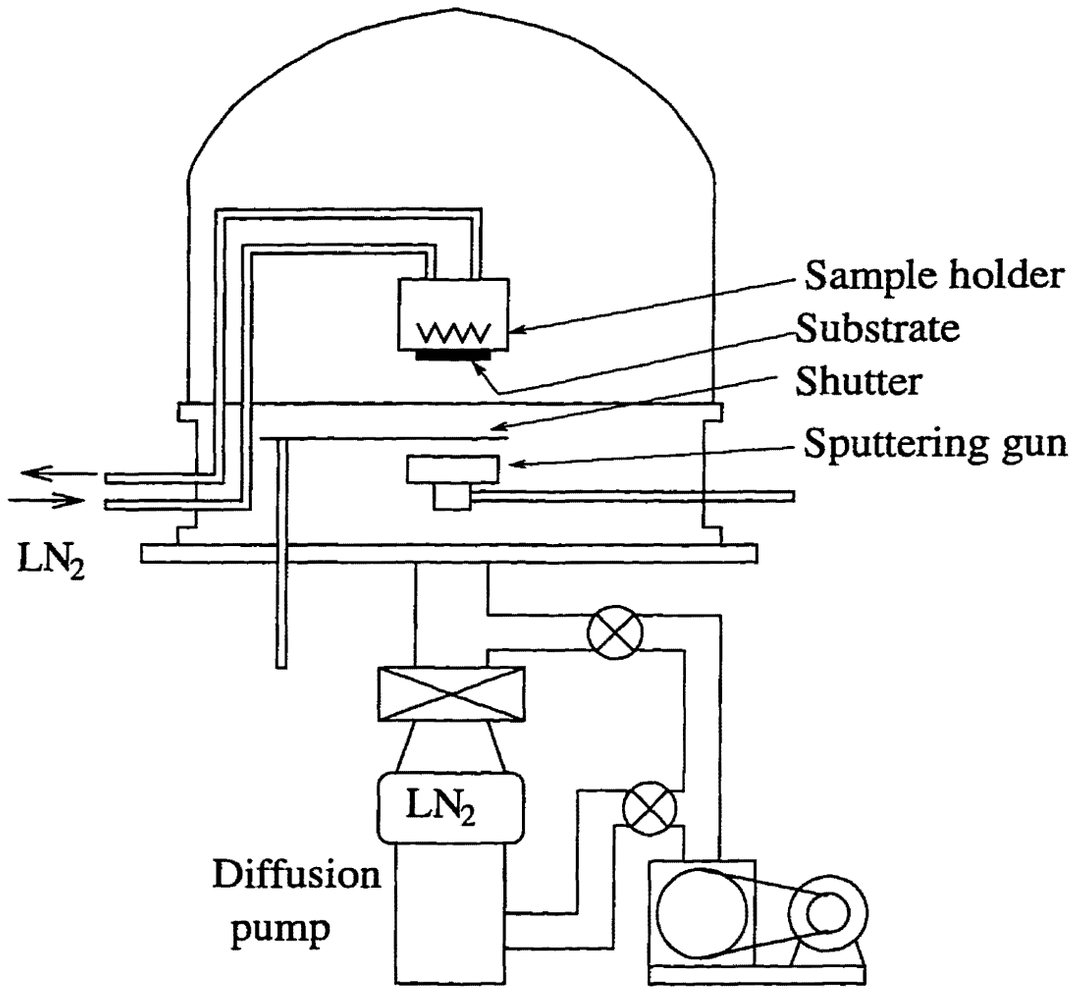


Figure 3.1: Sputtering deposition system.

high permeability Metglas target. The substrate holder has been designed with a capability of varying the temperature from that of liquid nitrogen to 500°C. The substrate temperature can be monitored by a thermo-couple.

Power (W)	100
Voltage (V)	450
Temperature (°C)	-196 – 500
Deposition rate ($\AA$/min)	130

Table 3.1: Deposition parameters.

The alloy composition of the film is accomplished by DC magnetron sputtering using a single target of the stoichiometric alloy made by vacuum melting. The target was supplied by Kurt J. Lesker Company. A moderate 450 V is used to prevent the reverse sputtering. The only possible volatile element in Metglas2605S2 is boron. To ensure the thin film has the right stoichiometry, Inductively Coupled Plasma (ICP) analysis has been performed, which confirmed that there is no deficiency in boron in our thin film samples.

3.3 Microstructures

To achieve an amorphous phase in metallic alloys, high speed quenching is required. This can be achieved experimentally by controlling the substrate temperature and sputtering power. Initial deposition trials were done at liquid nitrogen

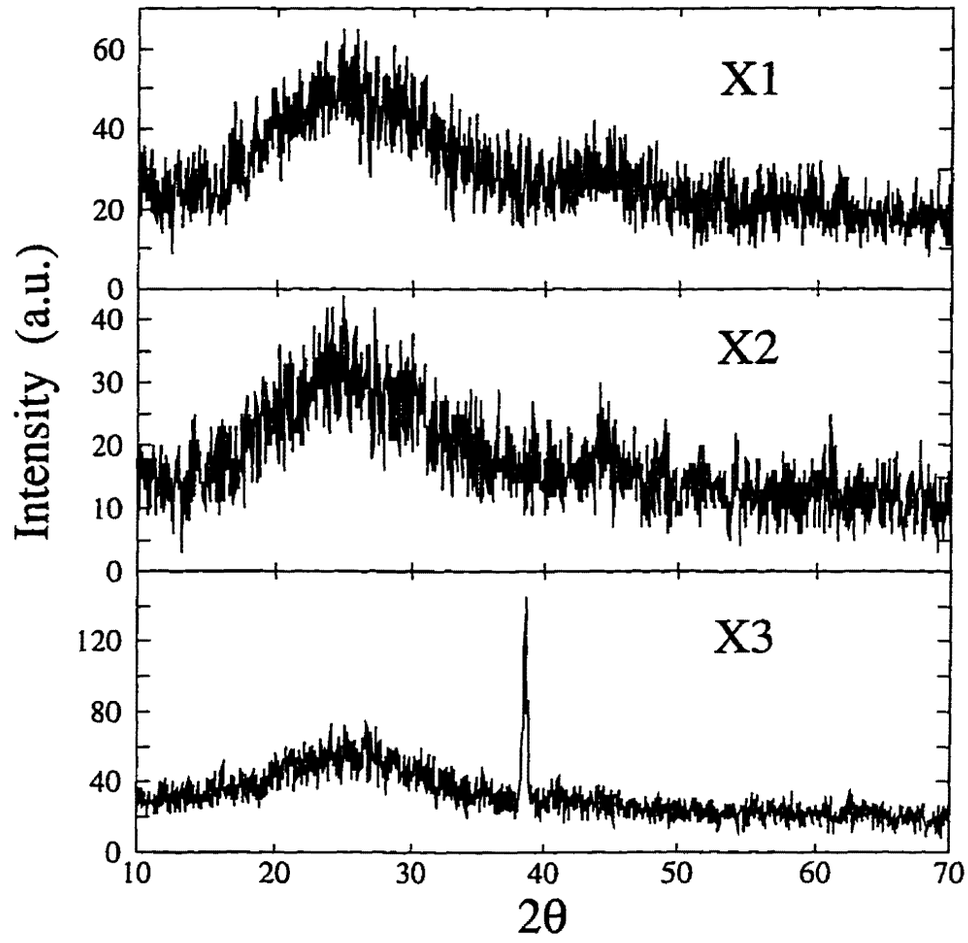


Figure 3.2: X-ray diffraction pattern of samples deposited at room temperature (X1), 300°C (X2) and 400°C (X3). X1 has been vacuum annealed at 500°C for one hour.

temperature to ensure an amorphous microstructure. Most samples in this work, however, are deposited at room temperature. Higher temperatures up to 400°C have also been tried to estimate the tolerance of the amorphous phase to substrate temperature. A low power of 100 Watts has been chosen to prevent the heating of the substrate by plasma. The substrates used for the studies of thin film properties were microscope cover glass slides of 150 μm in thickness. The deposition time was kept as 10 minutes; the deposition rate was 130 $\AA$ per minute.

X-ray diffraction (XRD) measurements have been performed to determine the deposition and post thermal processing boundaries for the amorphous phase. Of the three samples studied (see Fig.3.2), only X3, deposited at 400°C, shows a clear crystalline peak which might be attributed to Fe_3B. The amorphous phase is not only easy to achieve in Metglas thin films (up to 300°C), but it is also quite stable once formed. Thus, if the Metglas thin film is to be deposited on silicon at the end of an IC process, it should be able to survive the temperature of processing steps associated with die bonding and packaging.

3.4 In-situ magnetization

The key to the success of the thin film approach lies in the ability of defining the domain structure in-situ, as the film is being formed. Post field annealing on the Metglas thin film is found to be not as effective as its ribbon counterpart. This may be attributed to the difference in thermal expansion coefficients between the film and the substrate. Stress at the film-substrate interface will build up upon heating and cooling, pulling the magnetic domains away from the direction of mag-

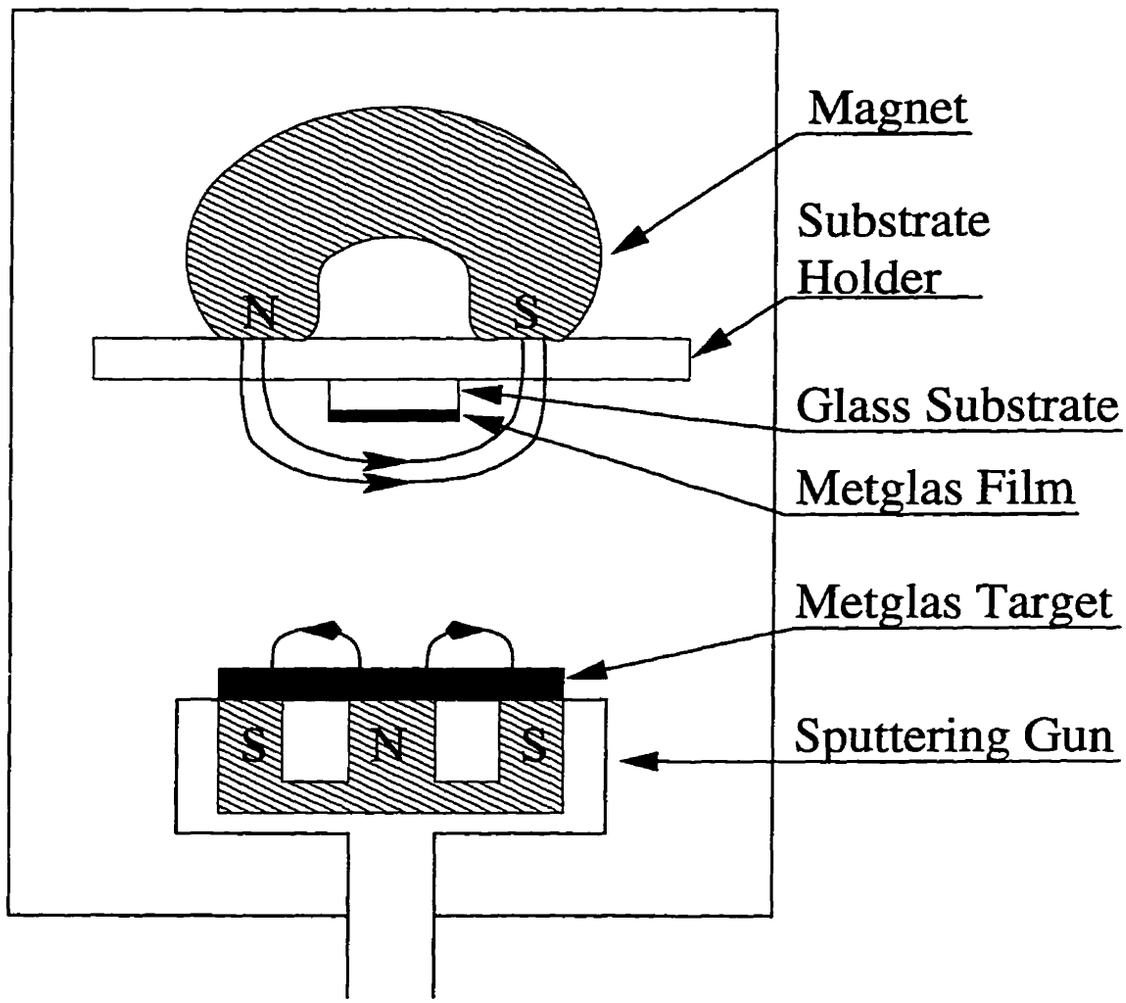


Figure 3.3: Magnetizing the thin film during deposition.

netization field. Hence the field annealing is not an efficient option for improving the magnetic performance of the thin film.

In-situ domain alignment at room temperature provides the only means of minimizing the thermal-expansion-induced interface stress. This is accomplished by placing a permanent magnet near the substrate to magnetize the thin film as the deposition process proceeds (Fig.3.3). The field at the midpoint of the horse shoe magnet is about 300 Gauss, and the substrates are placed 3.5 inches away from the target. At this distance, the residual magnetic field from the sputtering gun is about 30 Gauss, ten times less than the magnetizing field.

3.5 Magnetic characterization

To verify if the domains of the thin film have been successfully aligned during the sputtering process, a magnetization measurement has been performed on the as-deposited samples. The home-made curve tracer (Fig.3.4) used in this measurement is a simplied version of what has been used in [23] for thin film characterization. Basically, the thin film sample is placed inside a pair of Helmholtz coils, with its plane parallel to the applied magnetic field. The sample can be rotated around the axis perpendicular to its plane. A flat single-loop pickup coil, parallel to the sample plane, is placed at close proximity. The compensation coil is used to null the output before the sample is introduced. Instead of the B-H loop, our curve tracer measures dB/dt as a function of H. The B-H loop is then obtained by numerical integration. With a magnetic field of 320 A/m ($\sim$ 4 Oe) applied at 500 Hz, the largest dB/dt signal was found when the pre-magnetized axis of the sample was coincident with

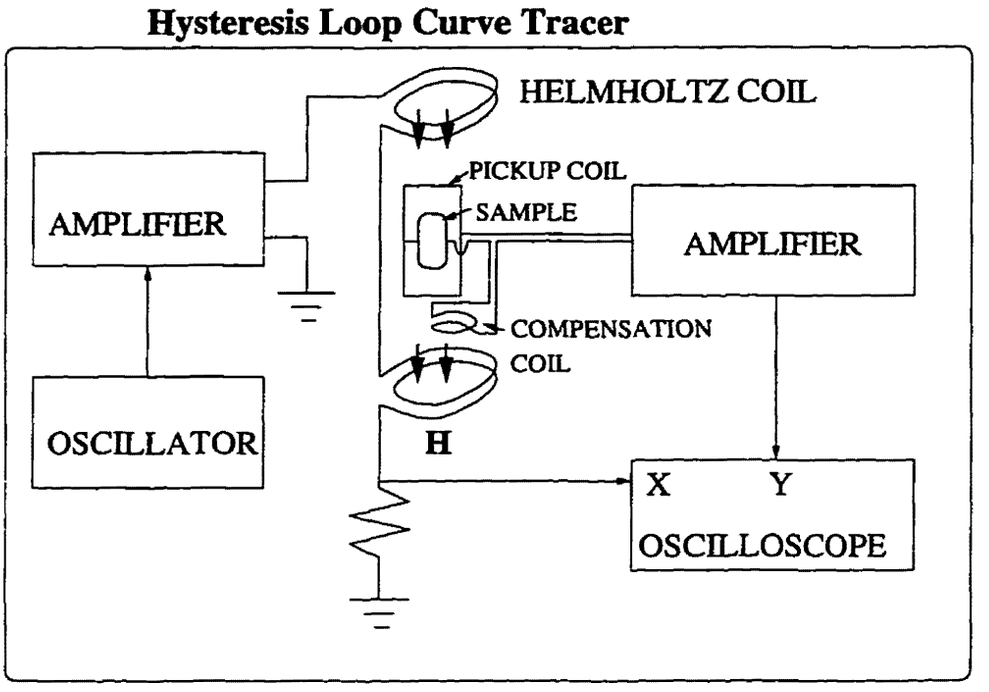


Figure 3.4: Measurement arrangement for characterization of the thin film B-H curve.

the measurement field direction (Fig.3.5). When this axis is orthogonal to the measurement field, no observable signal was found. This is a clear indication that the majority of the domains have been aligned by the magnetizing field during the deposition. The peak position in the dB/dt - H curve corresponds to the coercivity (Hc) of the material. The typical Hc in our room temperature deposited samples is around 1 Oe.

Once the easy axis is identified, the sample is further characterized for its magnetostriction properties using a capacitive measurement in the hard axis direction. As illustrated in Fig.3.6, a sample of 50 mm long (L), 20 mm wide (W) and 150 μm thick (t) is placed approximately 100 μm (D_o) away from another glass slide

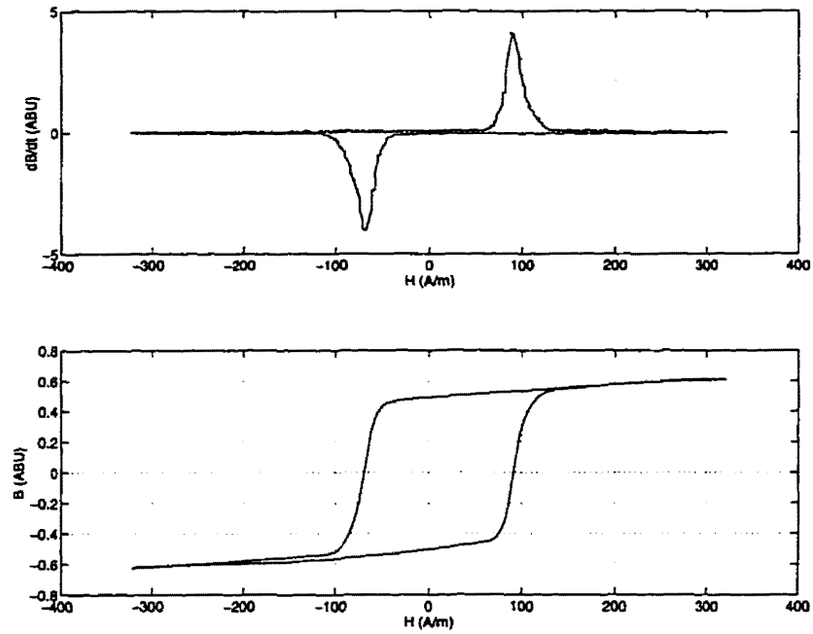


Figure 3.5: Experimentally measured dB/dt vs H curve of the as-deposited Metglas2605S2 thin film and the corresponding B-H curve obtained by numerical integration.

coated with Al. The sample is clamped at one end to form a cantilever beam. The average separation, D_o between plates is calculated using the standard relation

$$C_o = \frac{\varepsilon_o W L}{D_o}. \tag{3.1}$$

Here C_o is the measured value of the total capacitance before the magnetic field is applied and ε_o is the dielectric constant of vacuum. The magnetic field rotates the domains, elongating the film which leads to beam deflection. The deflection (D) of the beam with a thin film thickness, d, can be calculated using the following

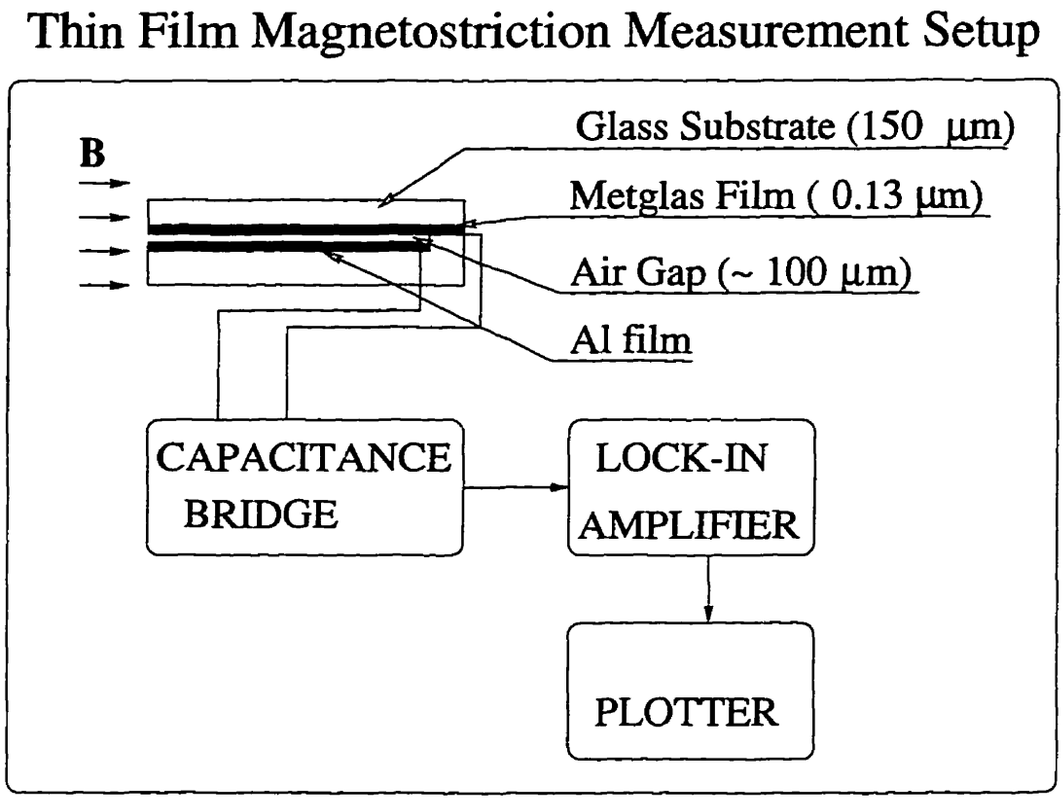


Figure 3.6: Capacitive measurement setup for thin film magnetostriction characterization.

equation [24]:

$$D = 3\lambda d \frac{E_f}{E_s} \frac{L^2}{t^2} \frac{1 - v_s}{1 + v_f}. \tag{3.2}$$

Here, E_f and E_s are the Young's moduli of the film and the substrate, respectively, v_f and v_s are the corresponding Poisson ratios, and λ is the strain induced in the film. L and t are the length and the thickness of the beam, and d is the thickness of the Metglas thin film. The material constants are listed in Table 3.2.

E_f [33]	1.7 x 10^{11} ($N.m^{-2}$)
v_f [33]	0.30
E_s [34]	0.73 x 10^{11} ($N.m^{-2}$)
v_s	0.17

Table 3.2: Young's moduli and Poisson ratios for Metglas thin film and glass substrate.

When the deflection D is much smaller than the zero-field separation D_o, we get

$$\frac{D}{D_o} = 3\frac{\Delta C}{C_o}. \tag{3.3}$$

The factor of 3 comes from the parabolic profile of the deflected beam.

In the measurement, the total capacitance C_o is retrieved by adjusting the bridge to null the output. The magnetic field is then applied, yielding an unbalanced output signal proportional to ΔC in the bridge. The strain, λ is obtained through equations (1)-(3) (see Fig.3.7).

To verify the compatibility of the thin film process with fibre-optic technology, Metglas has been deposited on optical fibres using the same deposition conditions. Details of the depositions and characterizations can be found in Appendix C.

Although the saturation magnetic strain, (λ_s) of 30x10^{-6} is comparable in value with the published data, the saturation field (Hs $\sim$ 15 Oe) and the coercivity (Hc $\sim$ 1 Oe) of the thin film are not as good as the field annealed ribbons (Hs $\sim$ 0.81). This may partly be attributed to the two inherent differences between the thin film and

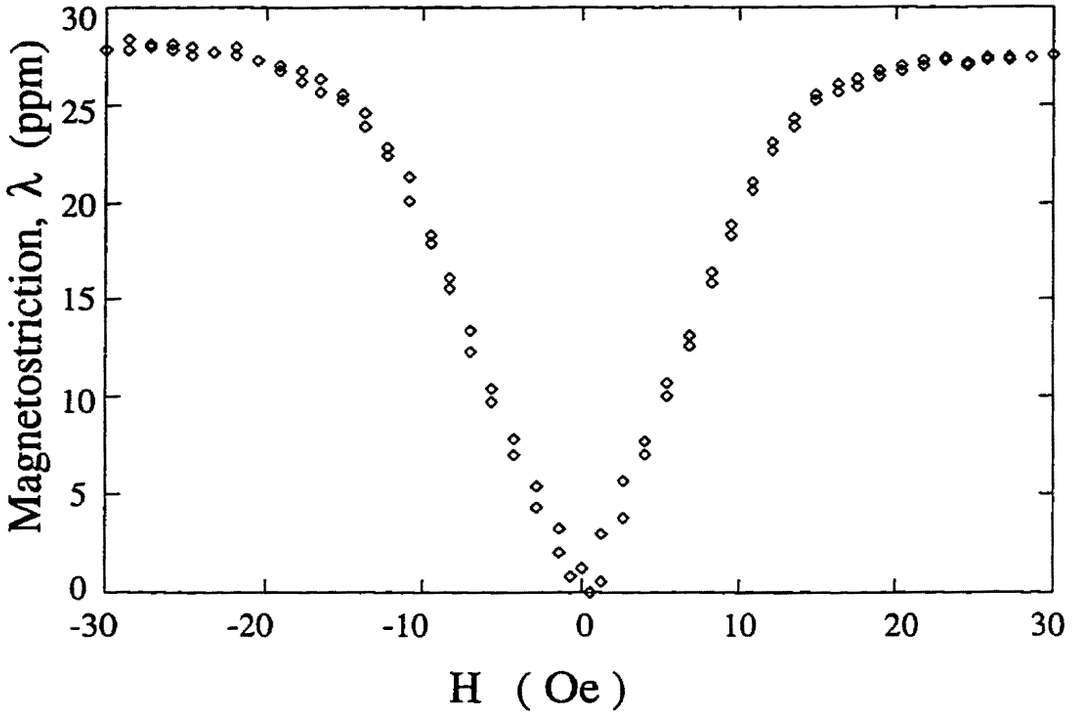


Figure 3.7: Measurement result of magnetostriction on Metglas thin film.

its ribbon counterpart; the Metglas film is much thinner and is mechanically coupled to the substrate. It has been reported for Metglas ribbons that the coercivity decreases with increasing thickness [25] because of wall pinning [26]. Nevertheless, the high value of Hs and Hc indicates that there might be internal stress in the film, due to the sputtering deposition process. Further investigations are needed with respect to deposition conditions, including the Ar pressure, sputtering voltage, deposition rate and possibly, the deposition temperature. If the saturation field were reduced to 1 Oe, an improvement of a hundred fold in sensitivity at low field could be expected.

In summary, we have developed a deposition process for Metglas thin films. The process allows easy control of the film composition and the amorphous structure needed can be achieved at room temperature. This has been verified by X-ray diffraction measurement. We have accomplished in-situ domain alignment in the film at room temperature by introducing a magnetization field during the deposition process. Magnetic measurements show that the Metglas thin film satisfies the basic requirements for magnetostrictive sensor device. Because of the low thermal budget of the deposition process, Metglas thin film can be implemented on IC wafers as the last deposition layer for smart sensor applications.

Chapter 4

Metglas thin film sensor and readout circuit

In this chapter, we present the design, fabrication and characterization of an IC compatible micromechanical transducer on silicon to take full advantage of the Metglas thin film technology developed. The design idea of the transducer comes from the thin film magnetostriction measurement described in the last chapter. Here, a miniature capacitor is realized on silicon, together with the MOSFET readout circuit, using IC process and IC materials. The glass cantilever is replaced by a low stress silicon nitride layer (passivation layer) to form the movable arm of the capacitor, while the fixed plate is made of a polysilicon layer (MOSFET gate). The air gap is realized by surface micromachining using Al metallization as the sacrificial layer (Fig.4.1).

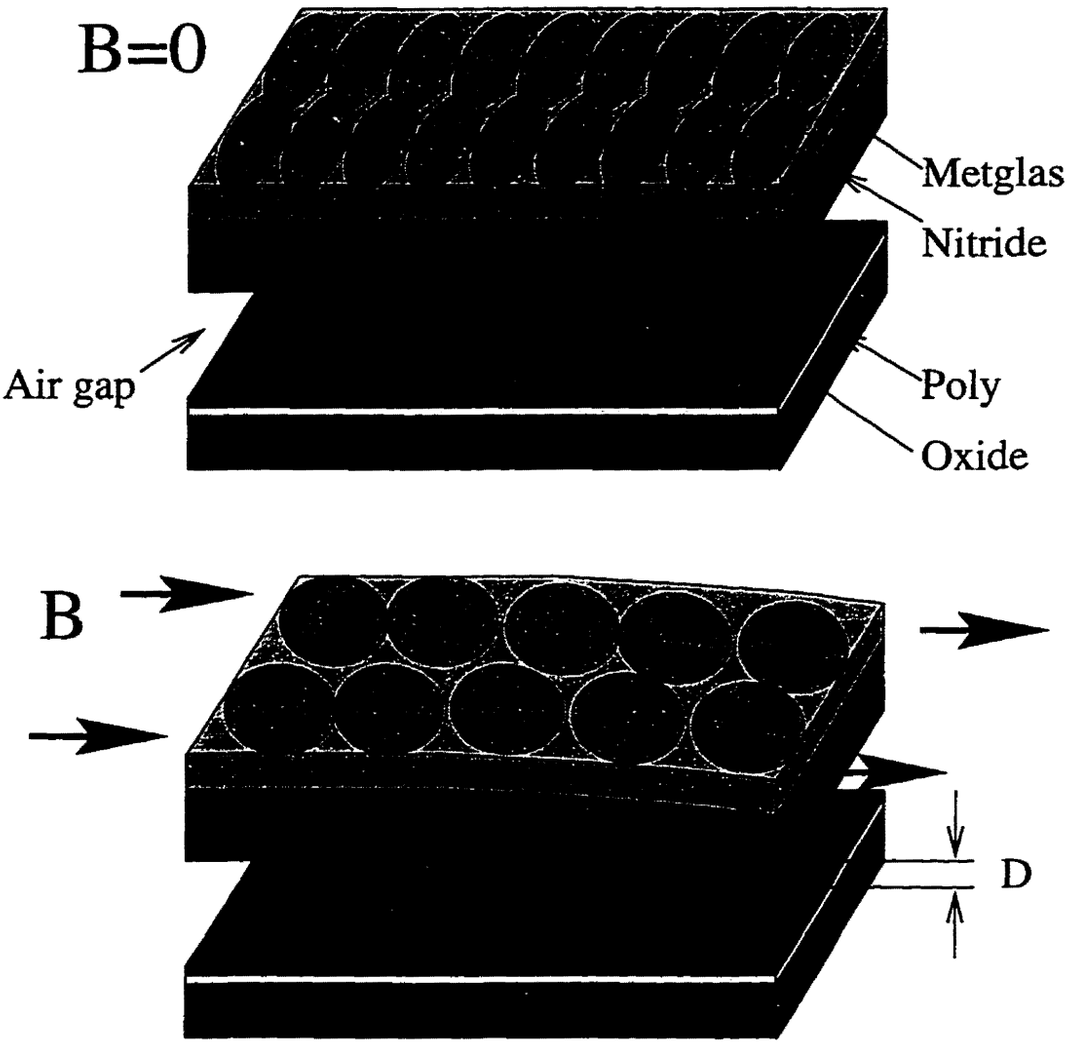


Figure 4.1: Operation principle of the IC compatible Metglas thin film sensor.

4.1 Design considerations

The magnetostrictive sensor to be fabricated is a two stage transduction device. The magnetic signal is first converted to a mechanical deflection through the composite Metglas thin film - silicon nitride cantilever beam, then measured as an electrical signal through the modulation of the capacitance. This requires design optimization in mechanical and electrical domains.

4.1.1 Mechanical consideration

The optimization of the mechanical response includes the enhancement of deflection D which is directly proportional to the sensitivity, and resonant frequency f_o of the beam. By operating at high frequencies, the $1/f$ noise is reduced. Both D and f_o are related to the dimensions of the beam [24, 2]:

$$D = 3\lambda d \frac{E_f}{E_s} \frac{L^2}{t^2} \frac{1 - v_s}{1 + v_f}, \tag{4.1}$$

and

$$f_o = 0.16 (\frac{E}{\rho})^{\frac{1}{2}} \frac{t}{L^2}. \tag{4.2}$$

Here E_f and E_s are the Young's moduli of the film and the substrate respectively, v_f and v_s are the corresponding Poisson ratios. ρ and E are the average density and average Young's modulus of the composite beam. d is the film thickness, L the beam length, t the beam thickness, and λ the magnetic field induced strain. These parameters are material related and fixed for a given process. Obviously, a large D requires a large L/t ratio. One interesting observation from Eq.(4.1) and (4.2) is that the deflection will remain the same when L and t are scaled down together,

whilst f_o is inversely proportional to the scaling factor. In another words, if the sensor were to be scaled down from what we used in thin film characterization (45 / 0.15 mm) to a miniaturized version on an IC chip (450 / 1.5 μm, for example), f_o would increase by a 1000 fold, going from 50 Hz to 50 kHz. In our actual design, the length (L) and the thickness (t) of the beam have been chosen as 400 μm and 2 μm. The glass cantilever beam has been replaced by nitride, leading to a revised $E_s = 3.85 * 10^{12}$ dyne/cm^2, $\rho = 3.1$g/cm^3 [39] and $v_s = 0.17$. These changes result in a f_o of 22 kHz. From mechanical point of view, L/t ratio should be as large as possible whilst their absolute value should be kept small.

4.1.2 Electrical consideration

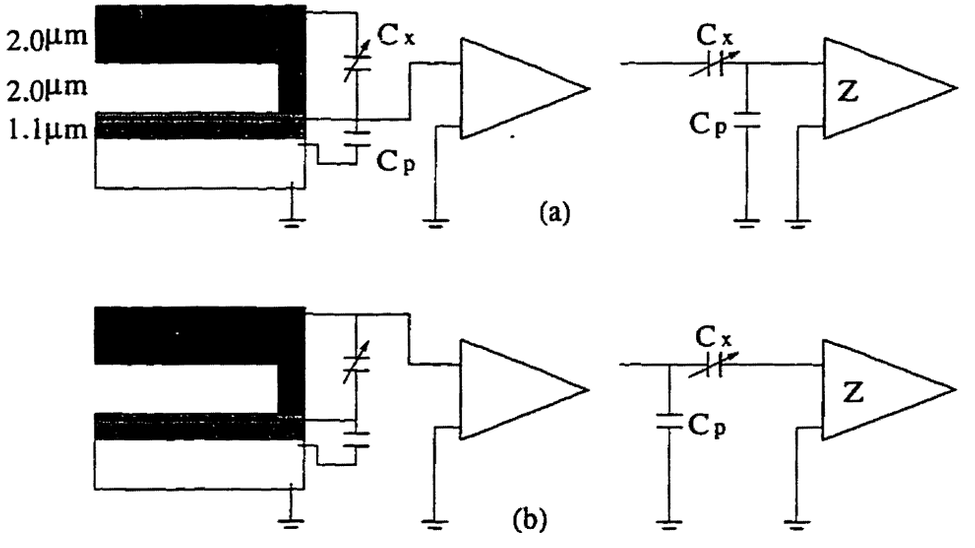


Figure 4.2: (a) poly fixed plate connected to the amplifier, (b) Metglas top layer connected to the amplifier.

Electrically, reduced cantilever dimensions lead to smaller sensor capacitance, making it vulnerable to parasitic capacitances between the sensor and the amplifier. In fact, the largest parasitic capacitance comes from the sensor fixed plate to the substrate (see Fig.4.2).

The ratio of C_p/C_x is determined by the thickness of field oxide, air gap and nitride. For the data given in Fig.4.2 (a), C_p is approximately 10 times larger than C_x. If the fixed ploysilicon plate were connected to the amplifier input (MOSFET poly gate) according to Fig.4.2 (a), the majority of the signal would be sunk to the ground. Fortunately, this problem can be overcome by flipping the connection as shown in Fig.4.2 (b). The next objective is to enhance the relative change in sensor capacitance $\Delta C/C_o$. This can be achieved by reducing the air gap D_o:

$$\frac{D}{D_o} = 3\frac{\Delta C}{C_o}. \tag{4.3}$$

However, the mechanically favored large L/t ratio and the electrically preferred small D_o pose serious challenges in terms of the fabrication process. The former reduces the stiffness of the beam while the latter increases the capillary force in the drying process after the wet etch; both lead to stiction problems. A compromise has to be reached between the sensitivity and fabrication yield. We have tested several cantilever beam thicknesses (1 μm, 1.5 μm and 2 μm) as well as air gaps (1 μm, 1.5 μm and 2 μm), using the same set of masks. High yield can be achieved when both t and D_o are 2 μm for a 400 μm long beam.

4.2 Sensor fabrication

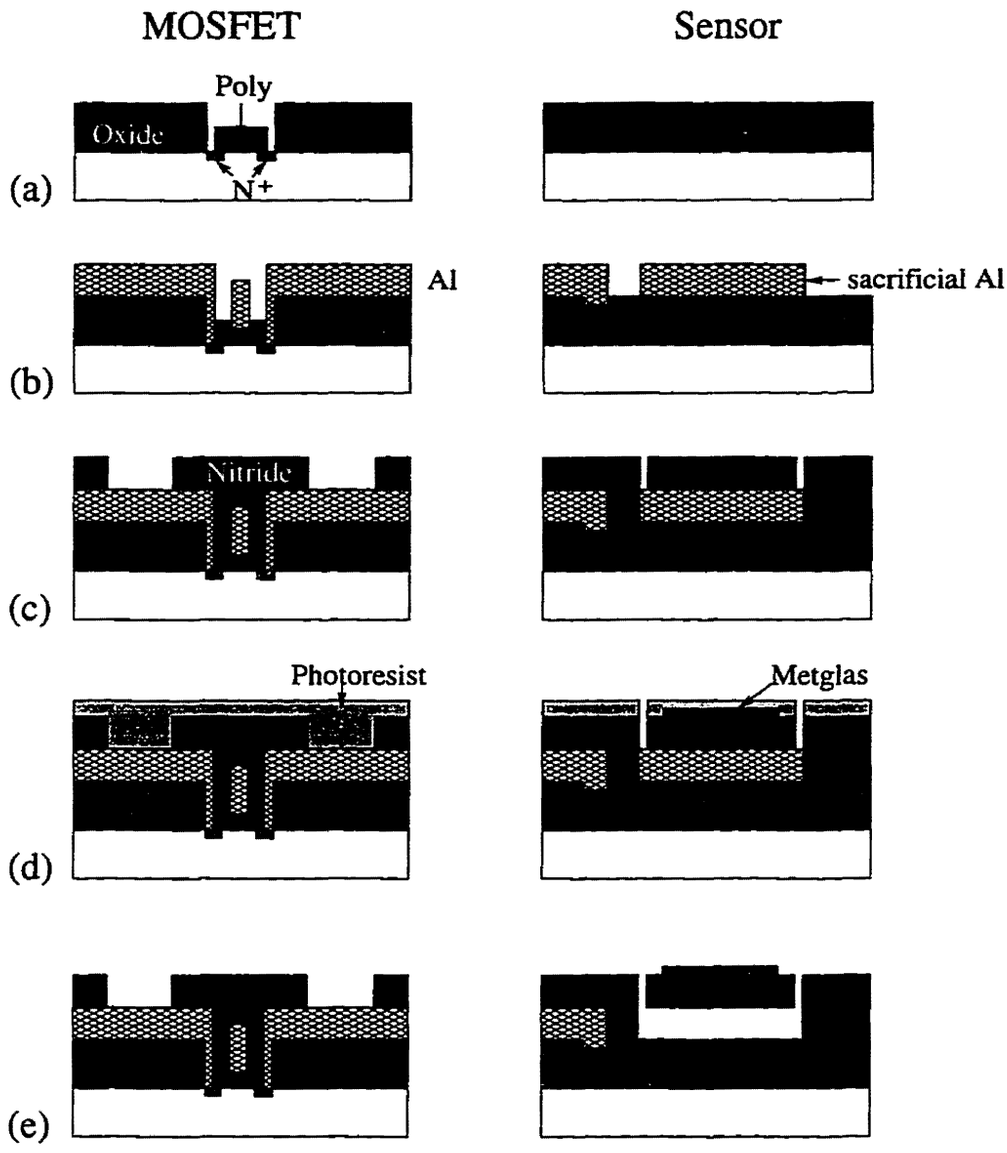


Figure 4.3: The fabrication process of MOSFET and sensor

The thin film Metglas sensor is fabricated using the in-house MOSFET process. Fig.4.3 (a) - (e) illustrate how the surface micromachined sensor is fabricated together with the MOSFET used for the readout. This is a 7 mask process, 5 for the MOSFET, 1 for the Metglas patterning and 1 for the surface micromachining. The mask set and the detailed fabrication steps are shown in Appendix A. Here briefly, P-type silicon wafers of 1-5 Ω cm (10^{16}) are used as substrate. The fixed plate of the sensor capacitor is patterned on field oxide using the same polysilicon layer as for the MOSFET gate. The Al metallization is also used as a sacrificial layer for a later surface micromachining step. The chip is passivated using low stress nitride, which also serves as the cantilever beam. On completion of the MOSFET process, the chip is protected by photoresist except at the etch windows on the sacrificial layer. The wafers are left in standard Al wet etch for one hour at 50°C to relief the cantilever beam. The dicing is carried out after the surface micromachining step, using photoresist as a temporary protecttion layer.

The finished sensors are shown in Fig.4.4 and Fig.4.5. The only add-on layer is the Metglas thin film, which is deposited at room temperature after the fabrication of the MOSFET. Only two more masks are needed for the sensor.

4.3 Sensor readout circuit

A major challenge for the success of the capacitive based Metglas thin film sensor lies in the signal readout. The typical size of the sensor is 400 μm x 100 μm with an air gap of 2 μm, which corresponds to a capacitance of 0.15 pF. The maximum deflection achievable is about 0.13 μm, or 3.3 fF in terms of capacitance change. If the device is to be used for measurement lower than the earth's magnetic field, the

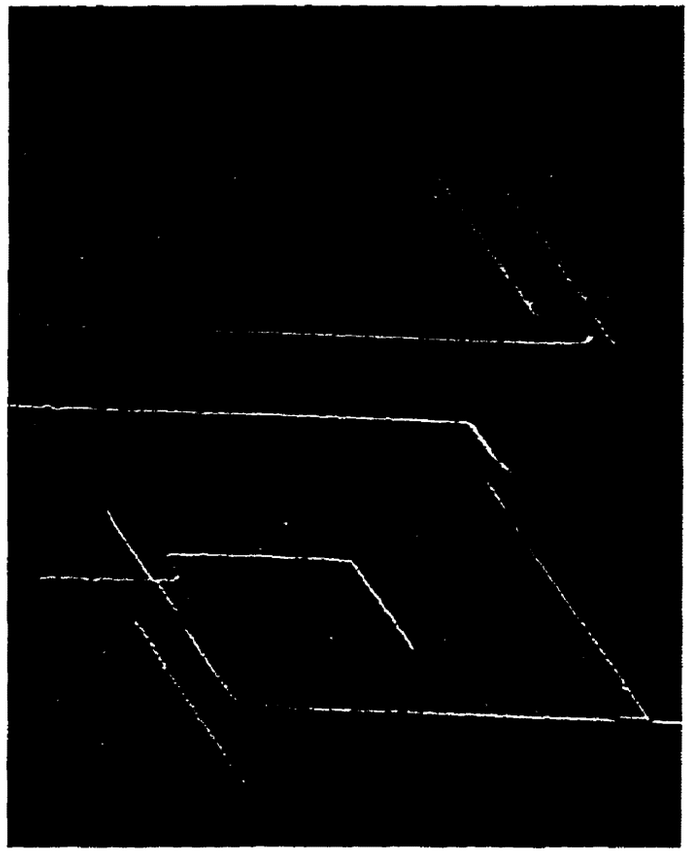


Figure 4.4: SEM of suspended cantilever beam with Metglas film (400 x 100 x 2 μm)..



Figure 4.5: Photograph of Metglas thin film sensor with readout circuit.

circuit needs to be capable of resolving beam deflection of a few $\mathring{A}$, corresponding to a few aF (10^{-18}F) in capacitance change.

Capacitive readout circuit can generally be classified into the following categories, capacitor bridge, inductor-capacitor (LC) resonator and switch capacitor circuit on an IC chip [35]. The resonator is difficult to be implemented with very small capacitors because it involves very high frequency, and requires a very high quality factor (Q) to resolve a small frequency shift. Conventional capacitive bridge circuit requires a perfect match of the sensor capacitance to that of the reference. This is difficult to realize in our case since it is hard to control the rest position of the surface micromachined cantilever beam to a great accuracy. The switch capacitor approach is very useful for on chip capacitive sensor readout, but it is quite involved in circuit design and signal processing.

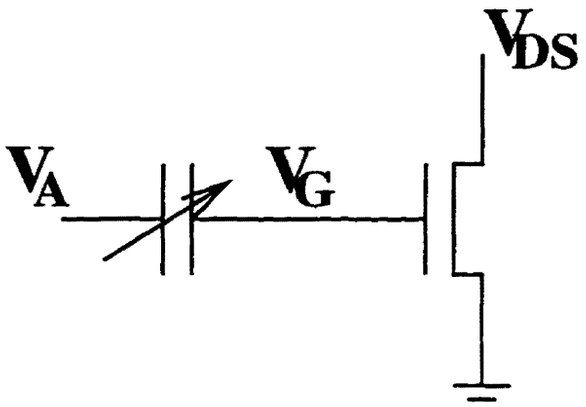


Figure 4.6: Floating gate configuration.

We propose here a simple readout scheme that provides the required resolution without critical requirements on the fabrication process or complexity in signal processing. We employ a charge coupled floating gate readout scheme (Fig.4.6). The sensor is connected directly to the gate of an enhancement mode NMOS. Instead of biasing the MOSFET gate using resistors, the DC bias is provided through the sensor, using the voltage dividing mechanism of the sensor capacitance and MOSFET gate capacitance. Here, the MOSFET gate capacitance does not have to match the sensor. Small deviations of the operating point due to the inaccuracy of the sensor capacitance can be compensated by adjusting the DC power supply to the sensor. The only AC frequency involved is the time dependent magnetic field signal to be sensed. The output is an AC voltage that is proportional to the cantilever beam deflection.

4.3.1 DC characteristics

The DC characteristics of the MOSFET without and with the sensor connected are shown in Fig.4.7 and Fig.4.8. Without the sensor, the MOSFET exhibits a standard transistor behavior, described by equation (4.4), with K of 0.071 mA/V^2, V_T of -0.3 V and V_A of 90 V,

$$I_{DS} = K(V_G - V_T)^2(1 + \frac{V_{DS}}{V_A}). \tag{4.4}$$

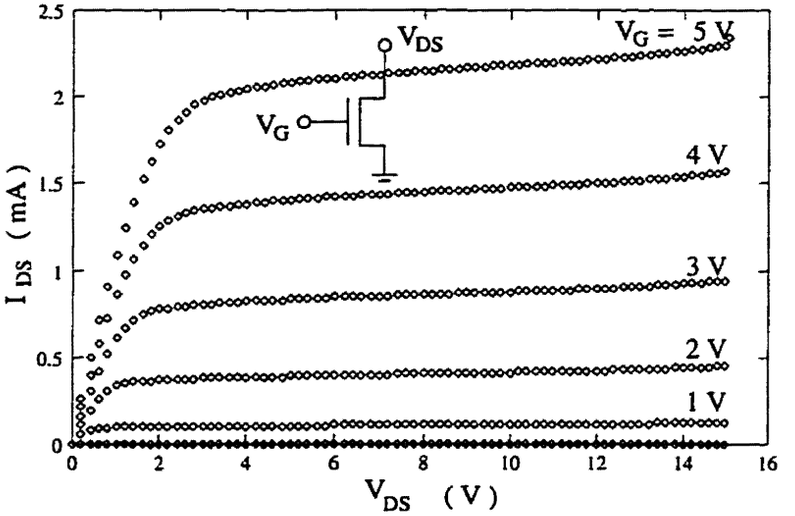


Figure 4.7: Current-voltage characteristics of the readout MOSFET without sensor.

With the series sensor capacitance, we note a reduced device transconductance as expected, because only a fraction of the voltage applied at the input drops on the gate. However, to our surprise, there was an increased current dependence on

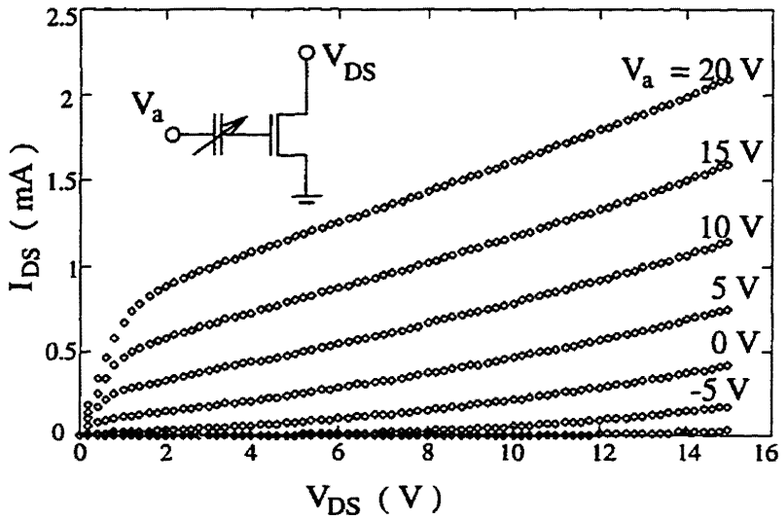


Figure 4.8: Current-voltage characteristics of the (sensor) charge coupled floating gate readout circuit.

source-drain voltage V_{DS} in the saturation region. A careful analysis which includes all parasitics shows that this is due to the gate-drain capacitance (see Fig.4.9), often referred to as Miller capacitance in device models [36, 37].

4.3.2 DC effects due to Miller capacitance

In standard circuit analysis [36] , the Miller capacitance is considered only at high frequencies in the common source mode, where it is responsible for the fall off of the gain. The 3dB frequency of the gain is determined by the RC constant at the input, where R is the resistance of the DC biasing network, and C is the sum of C_{gs} and equivalent capacitance C_{gd} at the input calculated using Miller's theorem.

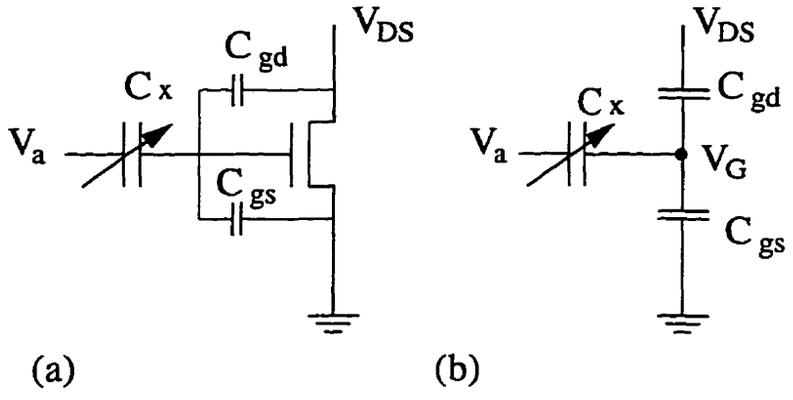


Figure 4.9: (a) Parasitic capacitances associated with MOSFET (b) DC equivalent circuit.

The key difference in the floating gate scheme is that there are no resistors connected to the gate. This implies a RC time constant that is infinitely large, which gives rise to a gain reduction that is observed even at DC. In fact, the Miller capacitance does not only affect the gain, but also changes the DC bias condition at the gate. As illustrated in Fig.4.9, the gate voltage V_G, is determined by

$$V_G = \frac{C_x V_a + C_{gd} V_{DS}}{C_x + C_{gd} + C_{gs}}. \tag{4.5}$$

Indeed, equation (4.5) yields good agreement with Fig.4.8, for MOSFET parameters and parasitic capacitances given in Table 4.1. The large value of the Miller capacitance, C_{gd} is related to our in-house NMOS process; the N^+ source and drain regions are realized using diffusion rather than implantation. This leads to large source-gate and drain-gate overlaps. The C_{gs} comprises three components:

the source-gate overlap capacitance, the gate-channel capacitance and the parasitic capacitance of the interconnect between sensor and gate. By design, the sensor capacitance is about half that of the gate-channel capacitance and the parasitic interconnect capacitance is about the same as that of the channel.

Table 4.1: MOSFET parameters and parasitic capacitances.

K (mA/V^2)	0.071
V_T (V)	-0.3
V_A (V)	90
C_{gd}/C_x	0.75
C_{gs}/C_x	4.5

4.3.3 Analysis of the circuit gain

We need to establish the relationship between the ac output voltage (v_{out}) and the change of sensor capacitance $\Delta C_x(t)$ due to the magnetic field H(t). Without considering the Miller capacitance, The analysis of the circuit is straightforward, since there is no coupling from output to input.

In that case, the total voltage on the gate, V_G can be expressed as

$$V_G = \frac{C_x + \Delta C_x(t)}{C_x + \Delta C_x(t) + C_{gs}} V_a. \tag{4.6}$$

Since $\Delta C_x(t)$ is much smaller than C_x, the above equation can be separated as time independent (DC bias, V_{G0}) and time dependent (AC signal, v_G) terms, using Taylor series. A linear expansion at the $\Delta C_x(t) = 0$ yields

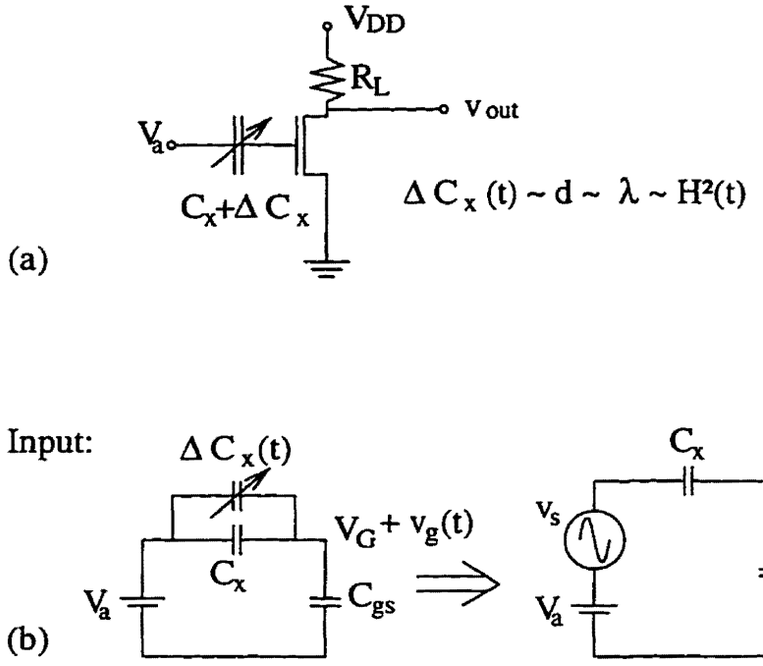


Figure 4.10: (a) Floating gate amplifier. (b) Converting ΔC_x to v_s at the input.

$$V_{G0} = \frac{C_x}{C_x + C_{gs}} V_a, \tag{4.7}$$

and

$$v_G = \frac{C_{gs} \Delta C_x(t)}{(C_x + C_{gs})^2} V_a. \tag{4.8}$$

An alternative way to look at the circuit is shown in Fig.4.10 (b). The variation of the sensor capacitance is equivalent to a small AC signal source v_s, and the high impedance nature of such a source is represented by the series connection of C_x. In small signal AC analysis, the DC voltage V_a can be considered as short circuit and the expression for v_s can be derived as

$$v_s = \frac{C_{gs}}{C_x + C_{gs}} \frac{\Delta C_x(t)}{C_x} V_a. \tag{4.9}$$

Now, let us look at the design considerations in determining the value of C_{gs} for the given C_x. From eq.(4.8), it seems that v_G can be enhanced by simply increasing V_a. This is misleading since V_a cannot be varied independently, without considering the DC bias of the transistor V_{G0}. Actually, the range of V_{G0} is fixed for a given technology, and V_a is varied to bring V_{G0} to the right range for different C_{gs}. Thus expressing v_G in terms of V_{G0},

$$v_G = \frac{C_{gs}}{C_x + C_{gs}} \frac{\Delta C_x(t)}{C_x} V_{G0}. \tag{4.10}$$

It is clear that increasing C_{gs} can enhance v_G when C_{gs} is smaller than or comparable to C_x, but at the cost of higher V_a (see eq.(4.7)). When C_{gs} is far larger than C_x, further increasing C_{gs} will saturate v_G at $(\Delta C_x(t)/C_x)\ V_{G0}$. Practically, C_{gs} should be chosen several times larger than C_x.

With equation (4.10), we can now estimate the capacitance resolution of the readout circuit. From our measurement, $C_{gs}/C_x = 4.5$, K = 0.071 mA/V^2, V_t = -0.3 V, given C_x = 0.15 pF, R_L = 7.5 kΩ, assuming V_{G0} = 3 V with an output noise level of 1 mV, the minimal $\Delta C_x(t)$ that can be measured is about 17 aF.

Now let's consider the effect of the Miller capacitance. In standard common source amplifiers where V_{G0} is determined by biasing resistors, C_{gd} only affects the AC gain at very high frequency. The small signal analysis can be conducted with a pre-determined transconductance, allowing the application of Miller theorem, which results in a very elegant scheme that decouples the input node from output. In the floating gate configuration, however, especially when C_{gd} is not small, the same decoupling scheme cannot be readily applied. In evaluating the impact of different parameters, we need to solve the following circuit equations:

$$I_D = \frac{V_{DD} - V_{out}}{R_L} \tag{4.11}$$

$$I_D = K(V_G - V_T)^2 \tag{4.12}$$

$$V_G = \frac{C_x(1+\alpha)V_a + C_{gd}V_{out}}{C_x(1+\alpha) + C_{gd} + C_{gs}}. \tag{4.13}$$

Where (4.12) and (4.13) are rewritten forms of (4.4) and (4.5). Here, $\alpha = \Delta C_x(t)/C_x$ denotes the relative change in sensor capacitance, and the slight dependence of I_D on V_{out} (V_{DS}) due to finite early voltage in (4.4) has been ignored,

which should not result in a big difference for this analysis. The goal of the following discussion is to evaluate the impact of C_{gd}, V_{DD} and V_a on the total gain of the sensor readout circuit. The exact solution has been derived (see Appendix D), but the expression is cumbersome thus failing to provide a simple physical insight. Instead of presenting the exact analytical solution itself, we show here the numerical results.

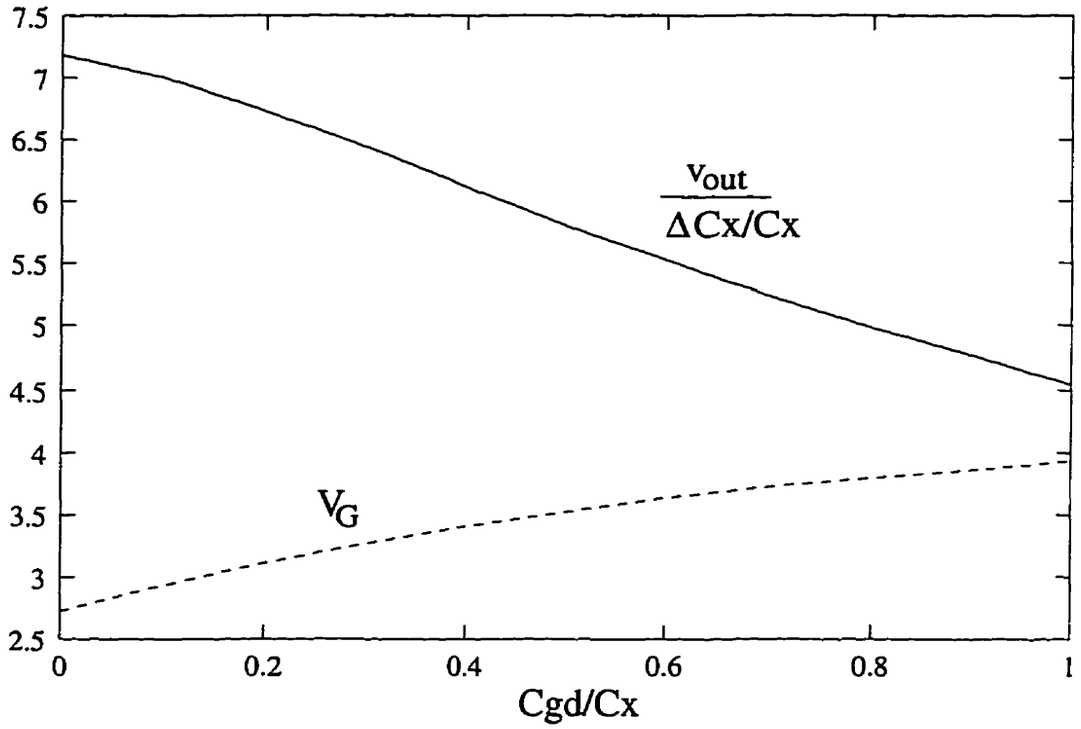


Figure 4.11: The dependence of gate voltage and AC gain on Miller capacitance.

Fig 4.11 is generated using the experimental data V_a=15 V, V_{DD}=20 V and MOSFET parameters given in Table 4.1. As C_{gd} goes up, the DC bias V_G increases, this alone should enhance the gain $v_{out}/(\Delta C_x/C_x)$. But this moderate enhancement is not enough to offset the associated negative feedback, resulting in

a net gain reduction. The revised capacitance resolution (with a noise level of 1mV at output) is about 30 aF, or 12$\mathring{A}$ in terms of beam deflection.

4.4 Magnetic field measurement results

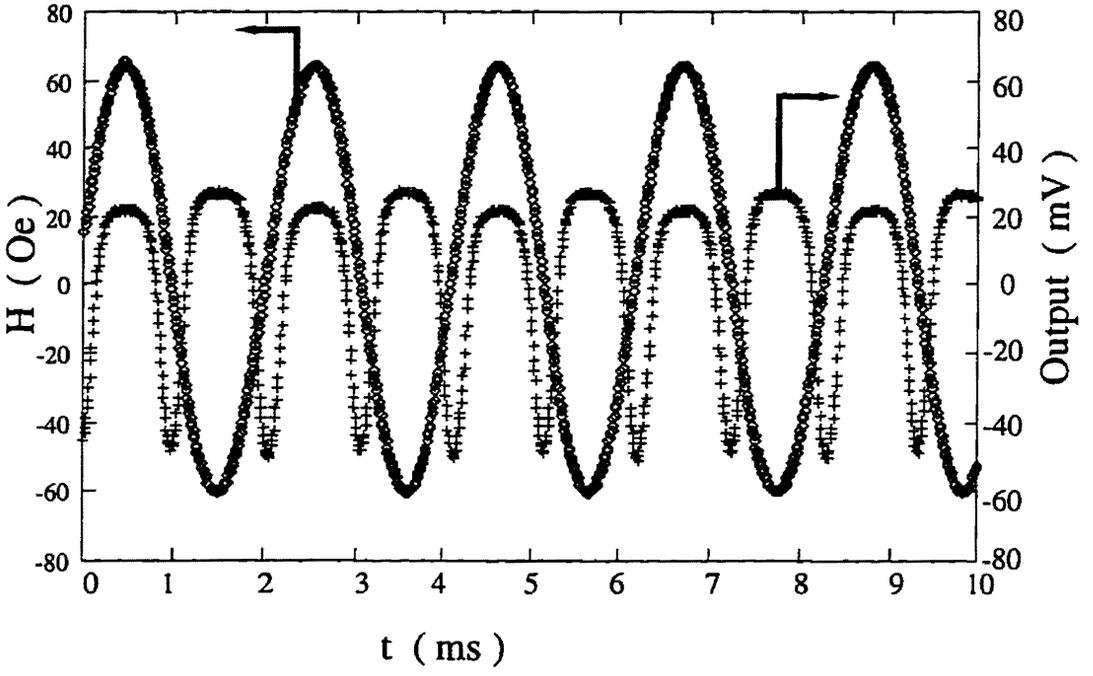


Figure 4.12: The applied field (H) and the output response for an AC magnetic field at 500 Hz, the output shown is obtained with an off-chip load of 7.5 kΩ.

In the magnetic field measurements, we apply a sinusoidal magnetic field of 60 Oersteds at 500 Hz. Since the frequency is far lower than the resonant frequency of the beam, the maximum beam deflection should be close to the static value of 1250$\mathring{A}$ according to previous calculation. A peak to peak output voltage of 70 mV

was observed, corresponding to a beam deflection of 1050$\mathring{A}$, which is of the same order of magnitude. The difference in values can be attributed to the variation of factors such as beam thickness and air gap.

Finally, a DC magnetic field has been applied to exploit the most sensitive part of the magnetostriction curve (Fig.4.13). The minimum detectable field (or magnetic field resolution) is determined by the noise level of the sensor system. Here, we observed a noise of 1 mV at output corresponding to a magnetic field of 0.4 Oersteds.

4.5 Discussion

Despite having addressed and resolved several key issues, our results are nevertheless preliminary. There is still room for further improvements.

4.5.1 Gain enhancement using advanced MOSFET

There are three major differences between our in-house MOSFET and advanced MOSFET process. Our fabrication technology has a larger minimum gate length, thicker gate oxide and a larger gate-drain overlap (or Miller capacitance), leading to a smaller transistor gain.

The transconductance of a MOSFET, is proportional to the gain, and can be described as:

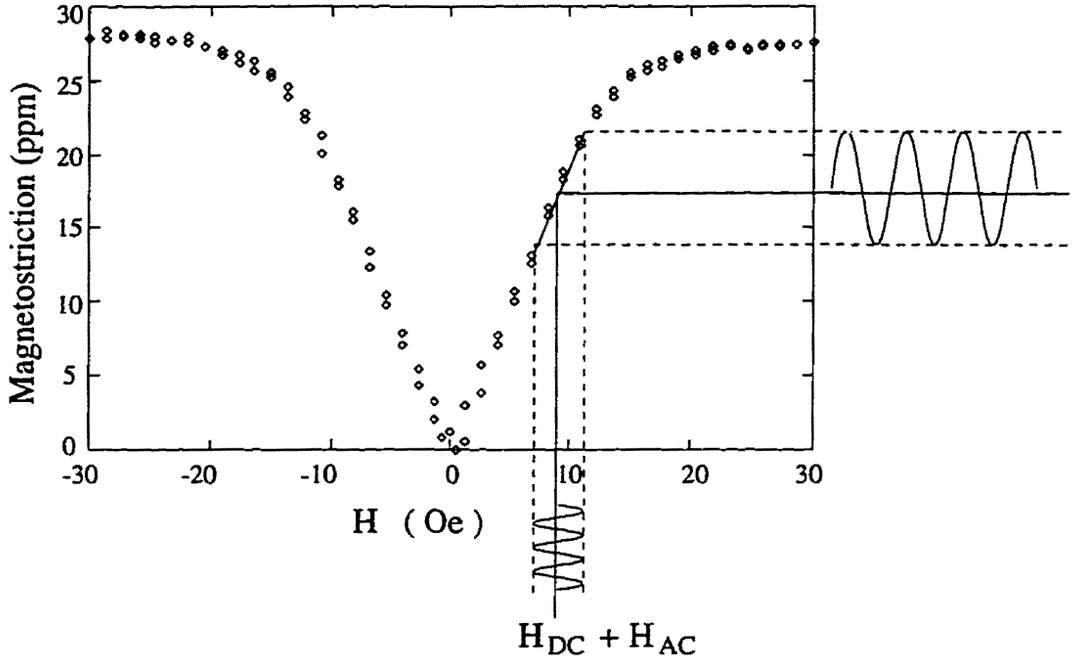


Figure 4.13: Strain induced in Metglas thin film as a function of the magnetic field H (1 Oe = 1 Gauss in vacuum). Small AC fields can be measured with a DC field bias.

$$g_m = \mu C_{ox} \frac{W}{L}(V_G - V_T) = \mu \frac{\epsilon\epsilon_o}{t_{ox}} \frac{W}{L}(V_G - V_T). \tag{4.14}$$

Here, μ is the carrier mobility in the channel, t_{ox} is the gate oxide thickness, L and W are the length and width of the gate. For a given sensor capacitance and DC voltage, the gate capacitance is fixed, assuming no parasitic capacitance:

$$Cgs = \frac{\epsilon\epsilon_o W L}{t_{ox}} = const. \tag{4.15}$$

Thus the difference in transconductance between a UW and and an advanced industrial MOSFET can be estimated. Assuming the same μ, V_G and V_T:

$$\frac{(g_m)_{ad}}{(g_m)_{UW}} = \frac{{L_{UW}}^2}{{L_{ad}}^2}. \tag{4.16}$$

Where $(g_m)_{UW}$ and $(g_m)_{ad}$ denote the transconductances of a UW and an advanced MOSFET, L_{UW} and L_{ad} are the corresponding gate lengthes. For $L_{UW} = 10\mu m$ and say $L_{ad} = 0.5\mu m$, we anticipate an sensitivity enhancement of a factor of 400 by using a state-of-the-art MOSFET process. In fact, we have designed test chips for fabrication using Nortel's 0.8 μm BiCMOS technology. Unfortunately, partial wafers are needed for post thin film deposition, lithography, and surface micromachining. Due to industrial restrictions, samples were not made available.

In addition to gate length, the Miller capacitance of a state-of-the-art MOSFET process is much smaller than our process. This will further improve the performance of the whole sensor system.

4.5.2 Non-magnetic packaging

Our sensor device is wire-bonded to a standard 24 pin packaging. These pins are made of gold plated nickel. The magnetic shielding effect of these magnetic pins can be observed clearly by comparing Fig.4.12 and Fig.3.7, which show apparent saturation fields of 40 Oe and 15 Oe respectively. Replacing the magnetic materials with non magnetic materials in package should be able to increase the sensitivity by a factor of 2 - 3.

4.5.3 Other applications of the floating gate readout circuit

The floating gate MOSFET capacitive readout technique developed in the current work is targeted for magnetostrictive magnetometers. It can easily be applied to any capacitive sensors, such as accelerometer and pressure sensors. There is also a growing demand to incorporate test structures on IC chips for process characterization and parameter extraction, particularly in new fabrication processes where low dielectric constant polymers being introduced as next generation insulators. The float gate technique can be an ideal test vehicle for evaluating small capacitor geometries with large fringing fields, uniformity of the dielectric material and Miller capacitances of the transistor [37].

The readout circuit finds applications also in chemical and biomedical sensing. For example, the Ion Sensitive Field Effect Transistor [38] (ISFET) has received great interests for measurements of PH and other chemical variables. In ISFET the gate polysilicon of a normal MOSFET is removed and the chemical solution is brought in direct contact with the gate oxide (sometimes, even the gate oxide

is replaced with aluminium oxide or polymers). With the floating gate technique, there may not be a need to disturb the gate oxide layer since it is vulnerable to factors such as contamination and instability. Any chemical manipulation can be done on top of the polysilicon gate. The required transduction of the chemical signal to the MOSFET can be achieved indirectly by transferring the chemically modulated charge through the gate ploysilicon.

Chapter 5

Conclusions and outlook

5.1 Summary of contributions

We have successfully prototyped a fully functioning thin film Metglas sensor on silicon that is co-integrated with a high resolution readout circuit. In the course of the thesis research, we have accomplished first results in the following two areas:

The deposition of Metglas thin film directly on a silicon substrate with built-in magnetic anisotropy in the pre-designed direction. To the best of our knowledge, this is the first report of its kind, and the technology is readily applicable to other magnetostrictive sensors developed previously, in particular, fibre optical interferometer based magnetometer. Researchers working on magnetostrictive ribbon sensors can benefit directly from the current work, with minor changes in terms of research infrastructures. In addition, the thin film technology has brought about new opportunities in IC compatible microsensor and microactuator applications. We have demonstrated the subsequent process integration with IC fabrication

technology. The Metglas thin film has been successfully integrated with micromechanical structures realized using surface micromachining with appropriate choice of sacrificial layer and low stress mechanical layers.

The development of a high resolution capacitive readout technique using a floating gate MOS transistor. The readout circuit requires only a single transistor that is operated either at DC or low frequency. Using the in-house developed prototype, we have successfully demonstrated that the circuit is capable of resolving 10^{-17} F (or a few $\AA$ in terms of cantilever beam deflection). This constitutes the current status of the technique. However, the circuit, through further optimization using an industrial IC process, is potentially capable of resolving sub atto Farads (10^{-18} F). With such a resolution potential, the floating gate readout technique can be applied to any capacitive sensors for on-chip readout. It is also an ideal vehicle for test structures on IC chip for process characterization and parameter extraction.

5.2 Future perspective

We have demonstrated many promising aspects of the integrated Metglas thin film sensor. Although major challenges have been resolved, there are plenty of opportunities to further advance the art. A number of the optimization issues which have been addressed separately in previous chapters will be further dealt with here.

Firstly, the saturation field of the Metglas thin film can be further improved through optimization of deposition conditions. One important parameter we have not changed in the current work is the film thickness, which is expected to affect the

domain structure. Direct imaging of the domain structure using polarized light or electron beam should aid in determining the optimal film thickness and deposition conditions. The Metglas thin film alone, can possibly provide an improvement in sensor sensitivity by a factor of 10.

Secondly, the gain of the MOSFET can be improved by over a factor of 100 using an industrial CMOS process, which offers a finer gate length and smaller Miller capacitance.

Thirdly, non magnetic packaging should be developed to replace the commercial packages which use gold plated nickel as pins. This should eliminate the effects associated with magnetic shielding and enhance the available magnetic signal to the sensor by a factor of 2 - 3.

Finally, the issue of noise should be investigated through measurements of the noise spectrum to identify possible noise sources for subsequent noise reduction by design. Since the high noise level of 1 mV was not observed in the MOSFET connected in a standard configuration where the gate voltage is well controlled using resistor voltage divider, we do not expect the noise to stem from the MOSFET itself. Equally, we do not expect the noise to stem from the sensor, since the small air gap damps off most of the mechanical vibrations of the cantilever beam. What may be the chief contributor to the noise is the long interconnect between the sensor and the MOSFET (see Fig.4.5). Because the MOSFET is connected in the floating gate configuration, the node of the MOSFET gate has a very high impedance, which is known to be vulnerable to ambient electromagnetic pick-up. Possible solutions include minimizing the interconnect length, on-chip shielding using the multilayer

metallization offered by modern IC processes, or off-chip shielding using special packaging.

Following the above considerations, it is possible to improve the overall performance (sensitivity and resolution) of the sensor system by as high as a factor of 1000, making the device very competitive to the fluxgate magnetometer, and even, its ribbon counterpart.

Appendix A

Fabrication sequence of integrated Metglas thin film sensor

A.1 Mask making

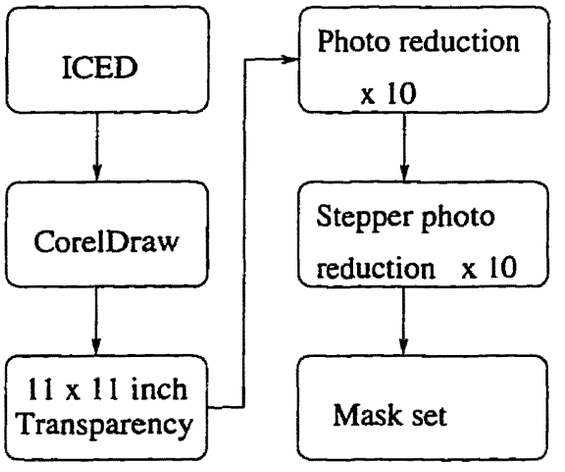


Figure A.1: Mask making flow.

The mask set in current work is designed and fabricated using in-house facilities. The design is done with a PC based CAD tool called ICED. The mask making process is illustrated in Fig.A.1. The overview of the mask set is shown in Fig.A.2, with each individual layer in Fig.A.3 to Fig.A.9.

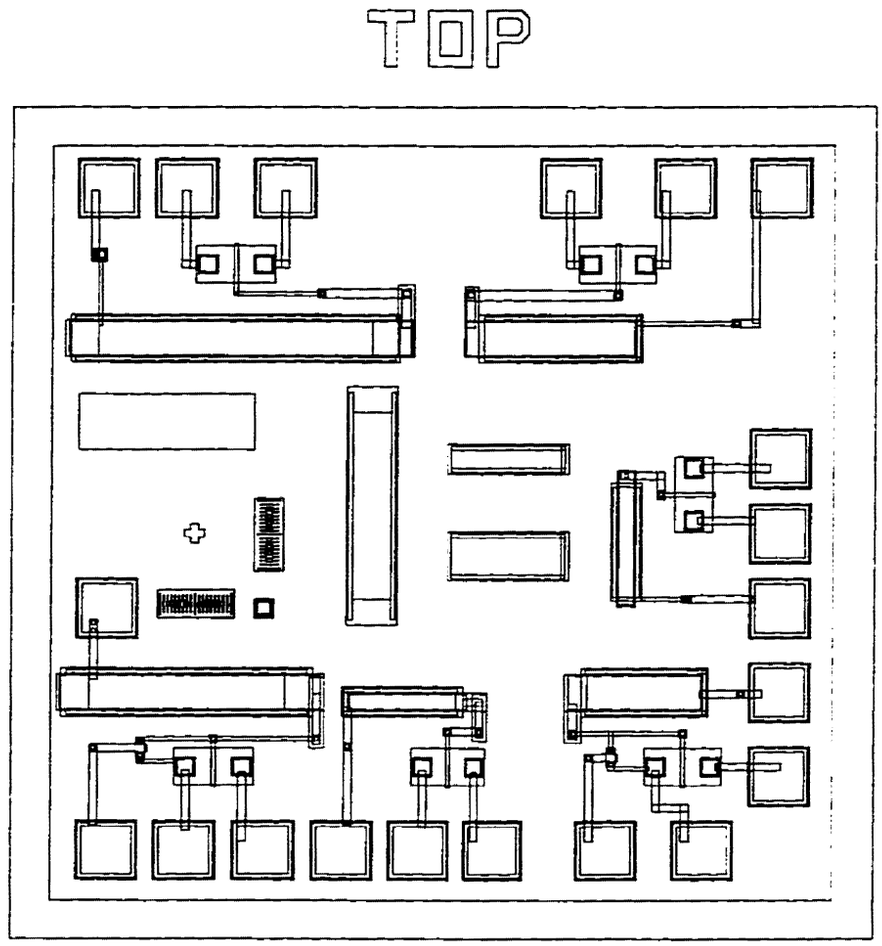


Figure A.2: Overview of the mask set.

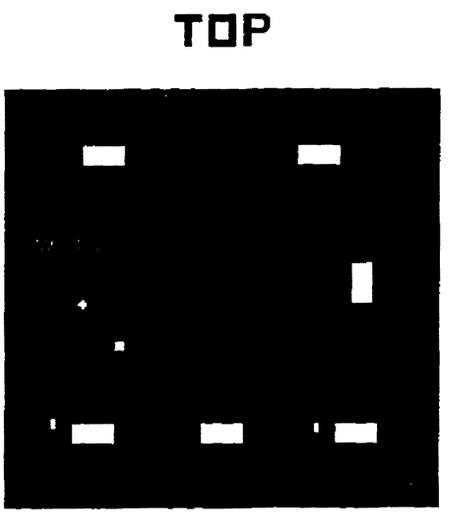


Figure A.3: Windows for gate oxide.

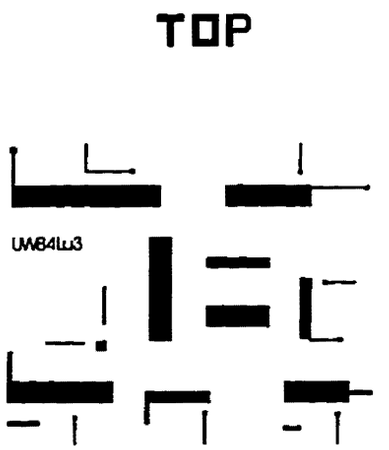


Figure A.4: Gate and sensor capacitor poly.

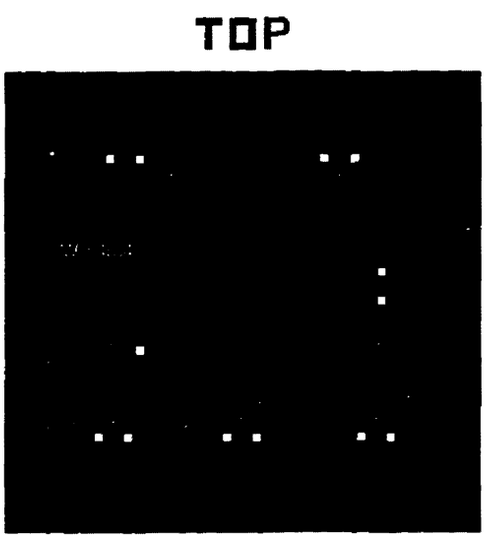


Figure A.5: Contact holes.

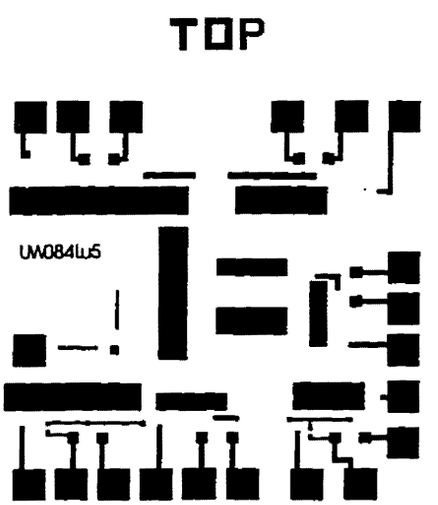


Figure A.6: Metal contact and sacrificial layer.

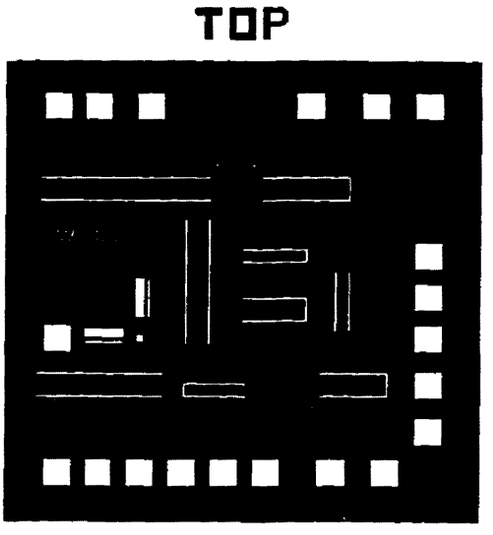


Figure A.7: Windows on passivation nitride for metal pads and sacrificial layer.

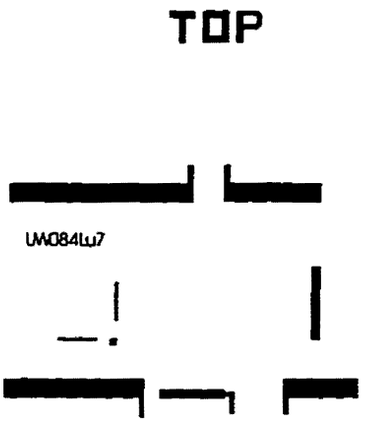


Figure A.8: Metglas pattern.

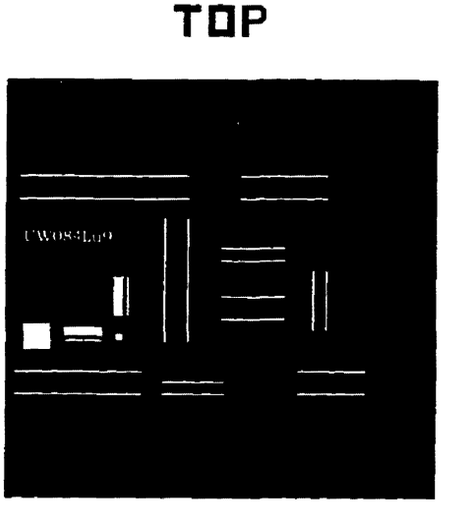


Figure A.9: Etching windows for sacrificial layer.

A.2 IC and sensor fabrication details

The wafer travel according to Fig.4.2 are listed in table A.1 and A.2. The key process conditions of various IC layers are listed in table A.3.

Table A.1: Process steps in Fig.4.2 (a).

	Fig.4.2 (a)
a1	Field oxide growth
a2	Open windows at MOSFET regions using mask #1 (UW084Lu2).
a3	Gate oxide growth: BHF (freshly prepared 20:1) dip right before the loading.
a4	Poly-silicon deposition.
a5	Poly oxidation: steam tube, 875°C dry O_2 5 min. (loading), 875°C steam 3 min., 875°C dry N_2 (annealing).
a6	Poly etch: pattern the poly oxide with mask #2 (UW084Lu3), strip photoresist, etch poly using KOH.
a7	BHF (8:1) etch, 2 min. for N^+ doping.
a8	N^+ (P) deposition: 950°C dry N_2 5 min. (loading, wafer back to back), 30 min. deposition, 3 min. N_2 flash, deglaze.
a9	LTO deposition.
a10	N^+ drive-in in: steam tube, 1035°C dry O_2 5 min. (loading), dry O_2 30 min., dry N_2 30 min.
a11	Open contact holes for metalization using mask #3 (UW084Lu4).

Table A.2: Process steps in Fig.4.2 (b) - (e).

	Fig.4.2 (b)
b1	Al deposition.
b2	Al patterning using mask #4 (UW084Lu5), standard Al etch.
b3	MOSFET testing #1, standard I - V, HP4145A.
	Fig.4.2 (c)
c1	Low stress silicon nitride deposition.
c2	Dry etch of nitride using mask #5 (UW084Lu6) on metal pads and sacrificial layer etch windows.
	Fig.4.2 (d)
d1	Metglas deposition.
d2	Metglas patterning, mask #6 (UW084Lu7).
d3	MOSFET testing #2, normal and floating gate configuration.
d4	Open window on sacrificial layer, mask #7 (UW084Lu9).
	Fig.4.2 (e)
e1	Al Sacrificial wet etch.
e2	clean the etching solution using boiling in DI water, clean photoresist using methanol - acetone - methanol rinsing.
e3	Apply photoresist to fix the beam temporarily on the wafer, dicing after soft and hard back of photoresis.
e4	Dissolve photoresist in acetone, then methanol, evaporate methanol quickly on a hot plate to prevent sticking.

Table A.3: Typical process conditions used in this thesis.

Process	Machine/Process conditions
Field oxide 1.1 μm	steam tube, 1100°C dry O_2 5 min. (loading), 1100°C stream 140 min.
Gate oxide 0.13 μm	gate oxide tube, 1100°C dry O_2 5 min. (loading), 1100°C dry O_2 48 min., 1100°C dry N_2 annealing 30 min. ramp down to 800°C in dry N_2
Poly-silicon deposition 0.30-0.31 μm	poly tube, 585°C, SiH_4 0.36 Torr, 28 min.
LTO	Corso-Gray Instruments Inc. 410 $°C$, 84 sccm SiH_4, 90 sccm O_2, 0.31 Torr, 350 W, deposition rate: 0.01 μm/min
Low stress nitride deposition 2 μm	AMC, PECVD 350 $°C$, SiH_4 + NH_3 + He. 180 min.
Dry etch (RIE) (AMC nitride)	Materials Research Corporation CF_4 20 sccm, 60 mTorr 350 V, 60 W, etch rate: 500Å/min
Aluminium deposition	Edwards Coating System E306A base pressure: 2×10^{-7} Torr, 100 sccm Ar, 5 mTorr, 400 W ,448 Volts 150 $°C$, deposition rate: 262Å/min
Al sacrificial layer wet etch	$H_3PO_4 : CH_3COOH : HNO_3 : H_2O$ = 456 : 36 : 18 : 90 cc, 50$°C$, 60 mins.
Metglas thin film sputtering deposition	upgraded Edwards vacuum Coating Unit base pressure: 2×10^{-6} Torr, Ar, 100 W ,460-480 V, DC, 300 Oe transverse magnetic field, room temperature, deposition rate: 130Å/min
Metglas thin film wet etch	Ceric Ammonium Nitrate 82.25 g, HNO_3 45 ml, add water to make 500 ml solution. room temperature, etch 0.13 μm in less than 30 sec.

Appendix B

Ferromagnetism, Magnetic domain and magnetostriction

We have shown the design, fabrication and characterization of Metglas thin film based magnetometer in Chapter 3 and 4. Most attention have been given to the mechanical and electrical considerations, with little coverage on the crucial magnetic issues. The candidate of magnetostrictive thin film material was chosen with a oversimplified two-parameter (λ_s, H_s) figures of merit. To further improve the device performance, an in-depth understanding of ferromagnetic material and magnetostriction is required. In particular, why amorphous materials have superior magnetoelastic properties than their crystalline counterparts, how the material properties change with mechanical, thermal, and magnetic processing. This appendix is intended to bridge that gap.

B.1 Ferromagnetism and Curie temperature

Ferromagnetism is the result of spontaneous alignment of microscopic magnetic moments in the substance. Strong ferromagnetic materials are usually composed of transition metals (TM) such as Fe, Co, and Ni, and rare earth (RE) elements such as Sm, Tb, and Ho, which are characterized by partial filled 3d and 4f shells, respectively. Since 3d and 4f electrons are close to the atomic cores and effectively shielded by valence electrons (s and p shells), they usually do not play an important role in the chemical bonding or electric conduction of the materials. They can be described, to a certain extent, with a localized atomic model (as opposited to the energy band model for s and p electrons) in which each (TM or RE) atom is regarded as a carrier of magnetic moment. Careful studies show that 3d electrons contribute only spins to the magnetization process, while 4f electrons contribute both spins and orbital moments. As a consequence, RE elements often show larger saturation magnetic intensity, M_s than TM elements.

Ferromagnetic material has been used since ancient times, but the microscopic origin of ferromagnetism was not understood for many years until the discovery of quantum mechanics [40, 41, 42]. With analogy to the bonding of hydrogen molecules, Heisenberg pointed out that the force responsible for the spontaneous alignment of magnetic moments (previously called molecular field) is not magnetic in nature. Rather, it is combination a Coulomb interaction and Pauli's exclusion principle. It was named as exchange interaction,

$$E_{ex} = J \sum_{ij} \mathbf{S}_i \cdot \mathbf{S}_j \tag{B.1}$$

Here, E_{ex} is the exchange energy, $\mathbf{S}_i$'s are spins of 3d electrons at different sites,

J is called the exchange integral, which is the measure of the interaction strength between neighboring 3d electrons. Ferromagnetism occurs only when J is negative, which indicates that the spin parallel state is energetically more favorable. Such a state is stable only when E_{ex} (or $|J|$) is larger than thermal energy, kT. At high temperatures, the alignment of the magnetic moment is vulnerable to thermal agitation; the material will experience a transition to paramagnetic state. The transition temperature is called the Curie temperature (Tc) of the material.

The interaction of 4f electrons is more complicated and cannot be accurately described by Heisenberg's theory. 4f electrons are so localized that their wave functions almost do not overlap with their neighbors. The magnetic moment coupling in RE elements is achieved through the help of spin polarized s, p, and d electrons.

It is important to note that: (i) the exchange force is a short range interaction that only nearest neighbors are important. This implies that polycrystalline and amorphous materials can be expected to have similar magnetic properties as their single crystalline counterparts, (ii) J is a function of distance between neighboring TM and RE atoms. Varying the atomic distance by alloying can dramatically change the value or even the sign of J. This helps to explain why alloying a material can have a great impact on the Tc.

The Curie temperature is an important parameter for applications. For instance, rare earth elements have large magnetic moments due to the orbital moment of 4f electrons, but none of them are considered strong magnetic materials at room temperature because of their low Tc's. Their alloys with TE elements, however, are most important magnetic materials especially for permanent magnet applications.

In selecting amorphous magnetostrictive ribbons, it is desirable to have a material whose Tc is well above room temperature but considerably lower than its crystallization temperature, so that field annealing can be performed near the Curie temperature without the risk of causing crystallization.

B.2 Magnetic anisotropy

In crystalline ferromagnetic materials, magnetic moments are found favor of certain crystallographic axes. Magnetization along these directions requires less energy from the external magnetic field. Accordingly, they are called easy axes (or directions). Magnetization curves of iron and nickel are shown in Fig. B.1.

Clearly, iron has its easy axis in $< 100 >$, nickel in $< 111 >$, and cobalt in [0001]. The preferential orientation of magnetic moments along certain directions in crystalline materials cannot be explained by Heisenberg's theory since the exchange energy only requires the neighboring spins parallel or antiparallel to each other, which have nothing to do with the crystallographic axes. This cannot be accounted for by magnetic dipole interaction either, since the magnitude of such an interaction is too small compared to experimentally obtained data.

Anisotropy in TM can be understood through spin-orbit coupling, the orbital motions of 3d electrons are asymmetric and the orientations of the wavefunctions (hence the charge distribution) are determined by Coulomb interaction with their neighbors. The spin "sees" the anisotropy and inhomogeneity of the wavefunction and adjusts its orientation accordingly to a low energy direction. When an external

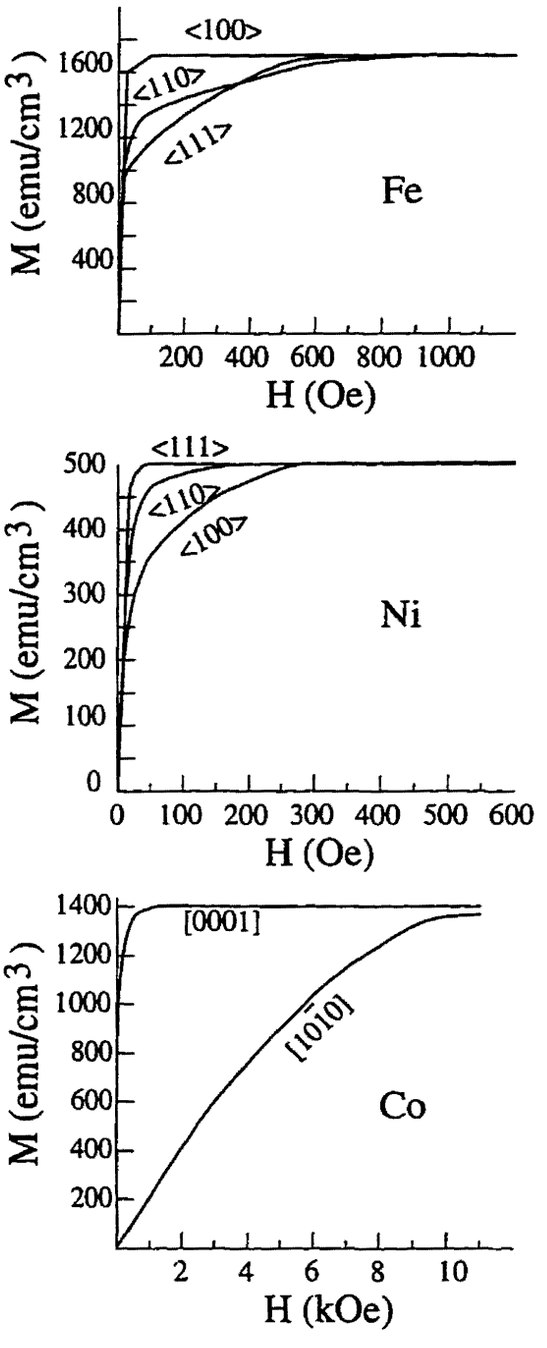


Figure B.1: The magnetization curve of Fe [43], Ni [44] and Co [45].

magnetic field is applied in a direction other than the easy axis, it tends to pull the spins away from their favorable orientation, causing an energy increase. The amount of energy required to completely align the magnetic moments with the field is called the anisotropic energy of the direction, which can be expressed in terms of the directional cosines (α_i) of the local magnetization M to the crystallographic axes. Taking the simplest lattice structure, cubic for example

$$E_a = K_0 + K_1(\alpha_1^2\alpha_2^2 + \alpha_2^2\alpha_3^2 + \alpha_3^2\alpha_1^2) + K_2(\alpha_1^2\alpha_2^2\alpha_3^2) + \cdots \qquad \text{(B.2)}$$

where the first term K_0 is the energy required to magnetize the material along its easy axis, which is mainly the energy required for domain wall movement. This term is often ignored in crystalline material since it is isotropic and relatively small. The higher order terms describe the angular dependence of the magnetization energy.

For rare earth materials, anisotropy can be understood in a similar way. The major difference is that the orbital moments of the 4f electrons also participate in the magnetization process. It is therefore not unexpected that they usually have a higher anisotropy energy. It is observed that most RE alloys have a H_a that is two orders of magnitude larger than that of TM elements.

The magnetic anisotropy is closely related to the symmetry of the system. In general, a low symmetry material system is more likely to have a high anisotropic energy. The materials having a highly symmetric cubic structure (Fe, Ni) for example, are usually expected to have lower anisotropy than the one having hexagonal (Co) or tetragonal structures. Polycrystalline materials are macroscopically

isotropic. But local anisotropy does affect the magnetization process. The magnetization curve for a polycrystalline material should lie somewhere between that of easy and hard axes of its crystalline counterpart, due to the involvement of domain rotations. This is equivalent to an increased K_0 term, but no direction dependent high order terms in equation B.1.

Amorphous alloys (3d-base) are "true" isotropic materials since there is no crystalline axis. The magnetic moment is no longer restricted by the "lattice", hence can choose its orientation according to local environment. K_0 can be orders of magnitude smaller than crystalline materials, this is why amorphous materials are usually easier to be magnetized. In amorphous material such as Metglas, the magnetostriction becomes the main reason of magnetic anisotropy. In fact, the macroscopic uniaxial easy axis can be introduced by annealing the sample at a temperature near Tc in a magnetic field. The anisotropic energy in a field annealed amorphous materials has a very simple form:

$$E_a = K_o + K_u sin^2\theta. \tag{B.3}$$

Here, θ is the angle between the local magnetic moment and the field annealing induced easy axis.

B.3 Magnetic domains

If only exchange and anisotropic energies were considered, ferromagnetic materials should have all spins aligned in one of the easy directions to form a macroscopic

moment **M**, *i.e.*, any ferromagnetic material should automatically be a saturated permanent magnet. This is of cause, not what is observed in the real world. A macroscopic moment will generate a magnetostatic field which carries a positive energy, E_M. To reduce the total energy, certain compromises have to be reached among E_{ex}, E_a and E_M. Nature chooses the following configurations for ferromagnetic materials:

(i) The material is divided into small domains, within which, spins are aligned along the local easy axis. Each domain can be considered as a small saturated permanent magnet. This satisfy the requirement of low E_{ex}.

(ii) Domains are separated by domain walls, which carry a positive energy, due to the no parallel spins across the domain wall. The thickness of the domain wall is determined by the competition among E_{ex}, E_M and E_a. The size and the orientation of domains are decided in such a way so as to minimize the magnetostatic energy without causing much increase in the domain wall energy and magnetic anisotropic energy.

Figures B.2 demonstrate how magnetic energy, E_M, is reduced when a large magnetic domain is divided into several smaller ones. Single crystal Fe forms a domain structure like that shown in Fig. 5.2 (d), while Co has domain structure of Fig. 5.2 (e), due to the strong uniaxial anisotropy along its hexagonal axis. The domains of closure are often observed at the surface of the magnetic materials, providing a closed loop for magnetic flux. The magnetic energy is, therefore, completely eliminated.

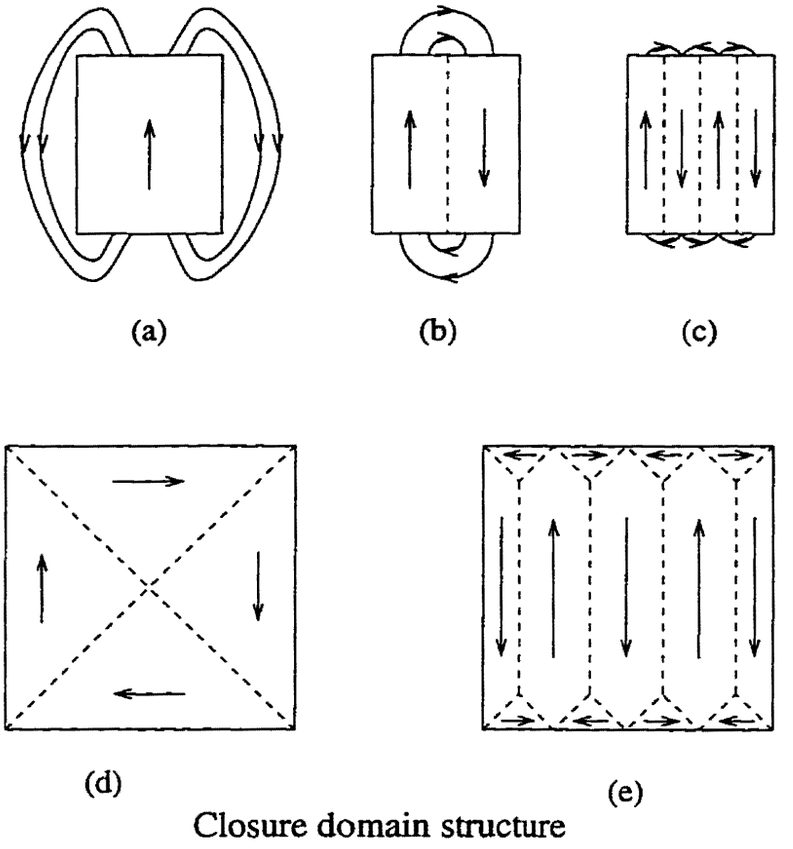


Figure B.2: The origin of magnetic domains.

B.4 Magnetization process

The magnetization process is the overall response of domains to the external magnetic field. Taking a single crystal sample as an example, the magnetization process can be divided into the following stages:

(i) At low fields, the domain walls can only be moved slightly away from the equilibrium position. The domain structure undergoes an elastic deformation, which

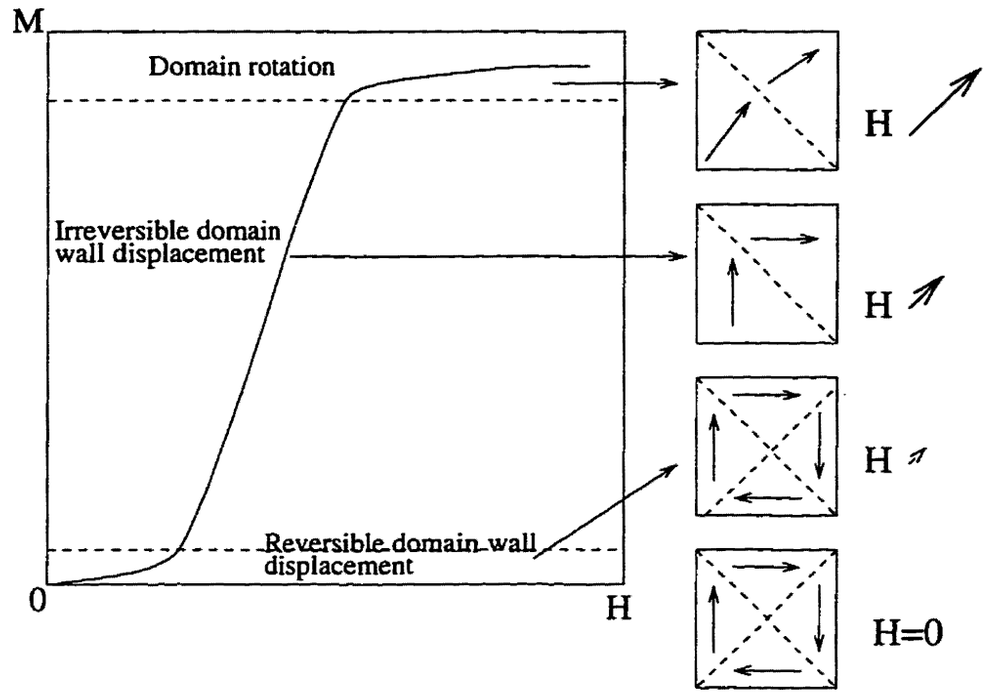


Figure B.3: Typical magnetization curve, showing the dominant magnetization processes in the different regions of the curve.

will be restored upon withdrawal of the external magnetic field.

(ii) In the intermediate field region, the magnetic field cannot overcome the anisotropic energy to rotate the magnetic domain, but it is strong enough to move the domain walls to increase the volume of domains parallel to the external field. Such a process causes an inelastic deformation, and the domain structure cannot be completely restored without the help of a reversal in magnetic field. The domain boundary movement is sometimes also referred to as a 180° domain rotation.

(iii) When the magnetic field is comparable or even higher than the anisotropy field, it will pull magnetic moments away from the easy axis. This process is called domain rotation (or sometimes, 90° domain rotation to distinguish it from 180° rotation, although the magnetic moments may not necessarily undergo a full 90° rotation).

The three regions are not clearly separated, *i.e.*, even at the low field region, a small amount of domain rotation can also take place. It is important to note that only 90° domain rotation is responsible for magnetostriction.

B.5 Magnetostriction

Magnetostriction is another property that is closely related to the anisotropy of the material. Kittel [42] pointed out that magnetostriction can be regarded as the dependence of anisotropy energy on the state of strain of the crystal. He extended the traditional analysis of E_a by including the strain related magnetoelastic terms. Under the new definition, anisotropy energy is not only dependent on the orientation of the saturation magnetic moment, **Ms**, but also on the interatomic distance, *i.e.*, the strain, *viz.*,

$$\begin{aligned} E_a &= K(\alpha_1^2\alpha_2^2 + \alpha_2^2\alpha_3^2 + \alpha_3^2\alpha_1^2) \\ &\quad + B_1(\alpha_1^2 e_{xx} + \alpha_2^2 e_{yy} + \alpha_3^2 e_{zz}) \\ &\quad + B_2(\alpha_1\alpha_2 e_{xy} + \alpha_2\alpha_3 e_{yz} + \alpha_3\alpha_1 e_{zx}) \\ &\quad + \frac{1}{2}c_{11}(e_{xx}^2 + e_{yy}^2 + e_{zz}^2) \end{aligned}$$

$$+\frac{1}{2}c_{44}(e_{xy}^2+e_{yz}^2+e_{zx}^2)$$
$$+c_{12}(e_{yy}e_{zz}+e_{xx}e_{zz}+e_{xx}e_{yy}).$$

Here, the first term is the traditional anisotropic energy, B_i's are magnetoelastic coupling constants and the last three terms describe the elastic energy of the material. The c_{ij}'s and e_{ij}'s are elastic moduli and strain. Without the magnetoelastic coupling ($B_i = 0$), the lattice should normally stay at a zero strain state. With the coupling, however, the strained state becomes the ground state. Thus a unit cell of, *e.g.*, cubic iron will automatically distort to a tetragonal below the Curie temperature. By minimizing the E_a with respect to strain,

$$\frac{\partial}{\partial e_{ij}}E_a = 0 \tag{B.4}$$

one can calculate the amount of distortion along each crystal axis,

$$e_{ii} = B_1\frac{c_{12}-\alpha_i^2(c_{11}+2c_{12})}{(c_{11}-c_{12})(c_{11}+2c_{12})}, \tag{B.5}$$

and

$$e_{ij} = -B_2\frac{\alpha_i\alpha_j}{c_{44}}. \tag{B.6}$$

The experimentally measured magnetostriction constants λ_{100} and λ_{111} can be related to coupling constants and elastic moduli by:

$$\lambda_{100} = -\frac{2}{3}\frac{B_1}{c_{11}-c_{12}}, \tag{B.7}$$

and

$$\lambda_{111} = -\frac{1}{3}\frac{B_2}{c_{44}}. \tag{B.8}$$

The dimension change under magnetic field can be visualized as in Fig. b.4, for the case of positive magnetostriction.

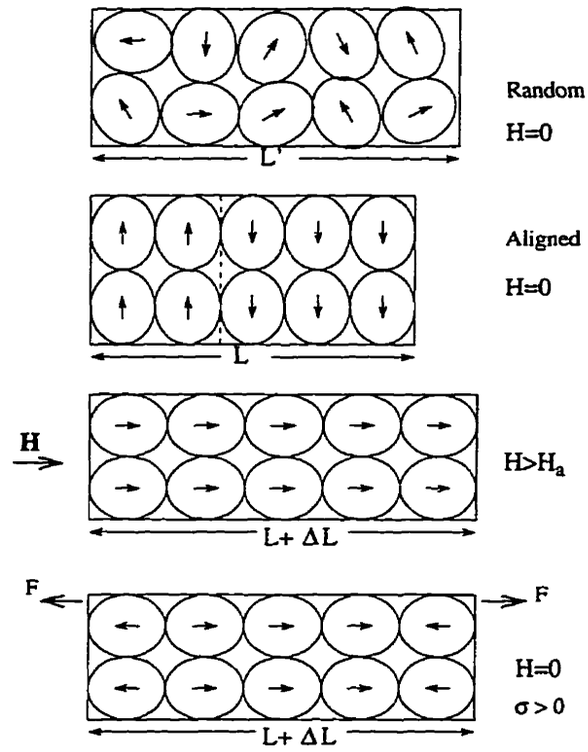


Figure B.4: The magnetostriction process.

From Fig. B.4, one can observe the following:

(i) Magnetostriction is closely related to the microscopic anisotropy, therefore, a low symmetry is essential for a large magnetic strain.

(ii) Magnetostriction is a direct result of domain rotation. The original orientation of domains is very important for determining the engineering magnetostriction. In particular, domains parallel or antiparallel to the magnetic field do not contribute to the dimension change at all, whilst domains that is perpendicular to the field contribute the most.

(iii) Stress can greatly affect the domain orientation and the easiness of domain rotation. This can result in dramatic changes in the magnetization as well as the magnetostriction process. Parameters such as permeability and coercivity are extremely sensitive to stress.

From the above and the discussions on anisotropy energy in previous sections, it seems that large magnetostriction(λ_s) and low anisotropy field (H_a) are conflicting requirements, *i.e.*, one cannot achieve both in the same material. Indeed, giant magnetostrictive materials such as $TbFe_2$ and $SmFe_2$ cannot be expected to be easily magnetized. The reason that Metglas can have a combination of large λ_s and low H_a is because the material has an unique symmetry; a moderate anisotropy at atomic level and very high symmetry at lattice level. It has been shown that even for giant magnetostrictive materials, making their structures amorphous is an effective way to reduce the saturation field.

B.6 Effect of stress and loading

The fabrication of the magnetostrictive ribbon sensor involves the bonding of a magnetostrictive ribbon onto a substrate, which is often accompanied by a stress at the interface between the magnetic material and the substrate. Such a stress is usually biaxial, due to the the curing of epoxy. Similar situation can also happen in Metglas thin film sensors, if the film is deposited at a temperature other than room temperature. Stress of this nature can disturb the magnetization process in two ways:

(i) For a negative magnetostriction material with a compressive stress (or positive magnetostriction and tensile stress), domains will be pulled away from the field annealed (or in-situ field aligned) direction, but stay in the plane of the ribbon. This will cause a deterioration of the engineering strain(λ_e) in the magnetic material.

(ii) For the compressive/positive or tensile/negative cases, stress tends to pull the magnetic moments normal to the plane. If the moments are originally aligned perpendicular to the plane, as in the case of surface crystallized ribbon, the stress is not going to do any harm to the domain structure, but it will hold the moments tighter in that direction, which is equivalent to an increase in the anisotropy energy, H_a.

In both cases, the stress has a negative impact on the sensitivity of the material by decreasing the effective magnetoelastic coupling constant, C_{eff}. Hence, any static interface stresses should be avoided whenever possible.

Even when there is no static stress at the interface, one has to consider the mechanical loading of the substrate. The magnetic field induced strain generated in the magnetostrictive material is coupled to the substrate through the interface stress. The stress will transfer part of the strain to the substrates, and at the mean time, counter-react on the magnetostrictive material. Hence the bonded material will appear magnetically harder than it is free standing.

Appendix C

Metglas thin film fibre-optic interferometer

As a first test of the thin film deposition technology, the Metglas was deposited directly on the optical fibre (see Table C.1 for the specification of the fibre and couplers used in this experiment).

Before the deposition, the plastic jacket of the fibre is stripped mechanically. Once stripped, the fibre becomes very fragile. The bare fibre is carefully mounted on a cylindrical sample holder (60 mm in diameter) for deposition of the thin film (see Fig.C.1). During the deposition, a magnetic field of 300 Oe is applied, and sample holder is rotated slowly. The Metglas film is coated only on one side of the fibre. The deposition conditions have been kept the same as in Chapter 3, except for the deposition time which is 60 minutes in this case.

The Metglas thin film coated fibre is measured using the setup shown in Fig.C.2.

	Fibre	Coupler
Manufacture	3M	E-TEK Dynamics
Part #	FS-SN-3224	SMFC9150AL811
Operating wavelength	630 nm	633 nm
	single mode	1 x 2, 50/50
Cladding Dia.	125 μm	125 μm

Table C.1: Specifications of fibre and couplers used for Metglas thin film fibre-optic interferometer.

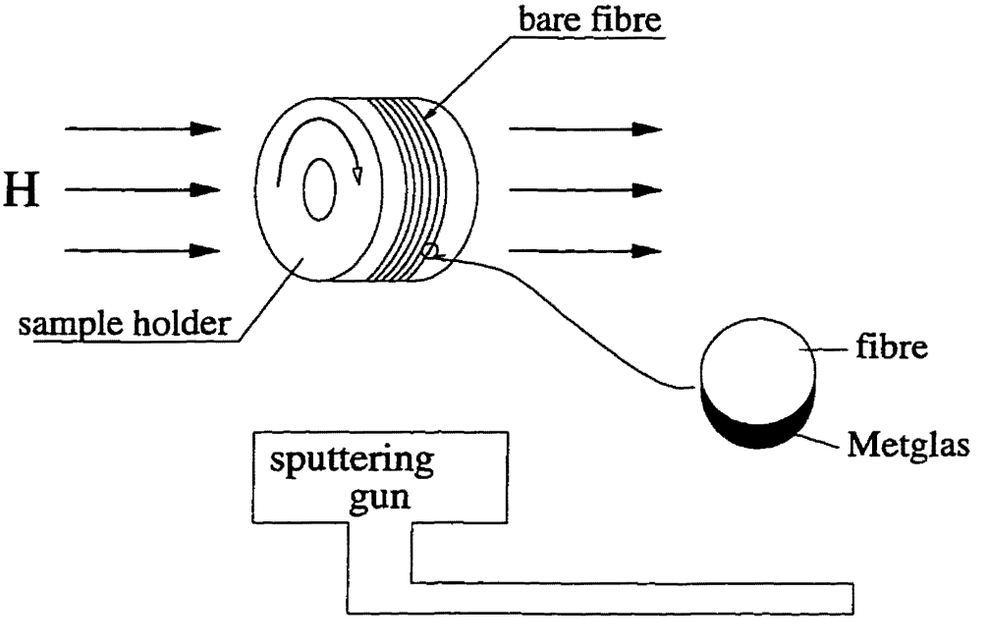


Figure C.1: Thin film deposition setup for optical fibres.

The light from a He-Ne laser (630 nm) is split evenly to the sensing arm (about one meter long) and the reference arm and recombined at the output by directional couplers. The length (hence the phase) of the sensing arm is modulated by a magnetic field generated by a coil 80 cm long. The photodetector measures the phase difference between the two arms. The measurement result is recorded by a digital oscilloscope.

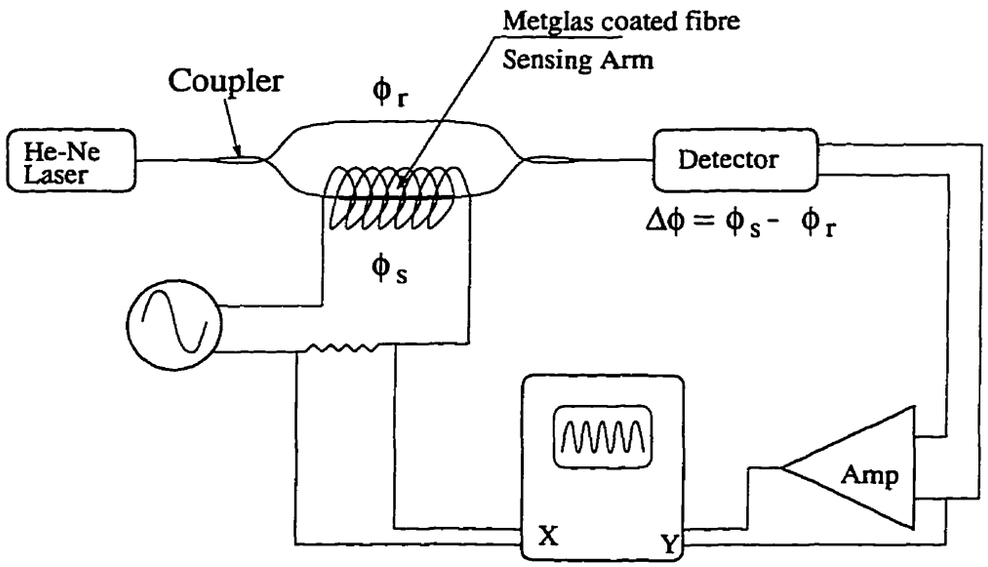


Figure C.2: Metglas coated fibre optic interferometer.

Illustrated in Fig.C.3 is the measurement result of the interferometer in response to a magnetic field of 60 Oe operating at 500 Hz. The frequency doubling of the output signal to that of the diving current is a clear signature of the magnetostrictive response of the Metglas thin film.

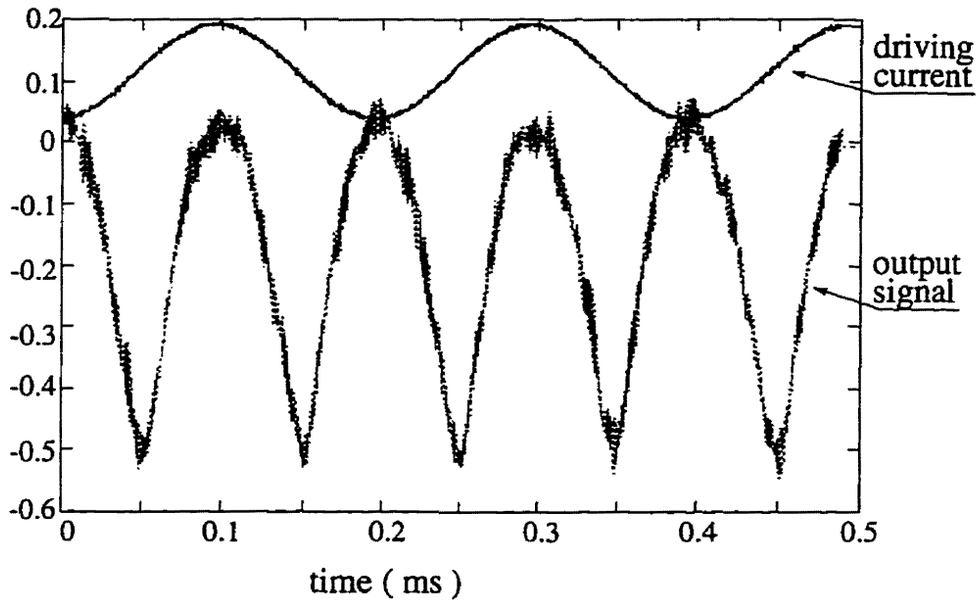


Figure C.3: Response of the Metglas coated fibre optic interferometer to a driving field of 60 Oe at 500 Hz.

Appendix D

Analytic expression of small signal voltage gain

The analytic small signal voltage gain is obtained by solving Eq.(4.11) - (4.13) using Maple. Here, the voltage gain is defined as the ratio of output voltage, v_{out}, *v.s.* the relative change of sensor capacitance, $\alpha = \Delta C_x / C_x$:

$$g_{cap} = \frac{v_{out}}{\alpha}. \tag{D.1}$$

V_{out} is solved first as a function of α, then expressed as a polynomial of α using Taylor expension. g_{cap} is the coefficient of the linear term of α.

$$g_{cap} = \frac{1}{2}(\,Cx + Cgs + Cgd\,)^2 \left(-2\,\frac{Cx\ Va\ Cgd}{(\,Cx + Cgs + Cgd\,)^2} \right.$$
$$+ 4\,\frac{Cx^2\ Va\ Cgd}{(\,Cx + Cgs + Cgd\,)^3}$$
$$+ \frac{1}{2}\,\frac{2\,Cx^2 + 4\,Cx\ Va\ Cgd\ K\ Rl + 2\,Cx\ Cgs + 2\,Cx\ Cgd}{K\ Rl\,(\,Cx + Cgs + Cgd\,)\,\sqrt{\%1}}$$
$$\left. - \frac{Cx\,\sqrt{\%1}}{K\ Rl\,(\,Cx + Cgs + Cgd\,)^2} \right) \Big/ Cgd^2 + (\,Cx + Cgs + Cgd\,)\,Cx$$
$$\left(-2\,\frac{Cx\ Va\ Cgd}{(\,Cx + Cgs + Cgd\,)^2} - \frac{1}{K\ Rl} + \frac{\sqrt{\%1}}{K\ Rl\,(\,Cx + Cgs + Cgd\,)} \right) \Big/ Cgd^2$$

$$\%1 = Cx^2 + 4\,Cx\ Va\ Cgd\ K\ Rl + 2\,Cx\ Cgs + 2\,Cx\ Cgd + Cgd^2$$
$$+ 4\,Cgd^2\ K\ Rl\ Vdd + Cgs^2 + 2\,Cgs\ Cgd$$

Bibliography

[1] K.D. Wise, *Integrated sensors: Key to Future VLSI Systems*, Proc. 6th Sensor Symp., 1-9(1986).

[2] S.Middelhoek, S.A.Audet, *silicon sensors* Academic Press Inc. (1989)

[3] J.E.Lenz, *A Review of Magnetic Sensors*, Proc.IEEE. **78**, 973-989(1990)

[4] *Applied Metglas Products specification Sheet*, Allied Signal Inc., Metglas, Parsippany, N.H., 1989

[5] A.D.Kersey, D.A.Jackson and M.Corke, *Single-Mode Fibre-Optic Magnetometer with DC Bias Field Stabilization*, J. Lightwave Tech.**LT-3**, 836-840(1985)

[6] B.J.Lynch and H.R.Gallantree,*A New Magnetic Sensor Technology*, GEC J.Res.**8**, 13(1990)

[7] J.H.Vincent, A.P.Thomas and M.R.J.Gibbs, *Magnetostriction in Surface Crystallized Metallic Glasses*, GEC J.Res. **10**, 179-184(1993)

[8] Y.Lu and A.Nathan *Metglas thin film with as-deposited domain alignment for smart sensor and actuator applications* Appl. Phys. Lett. **70** (4) 526-528 (1997).

[9] Y.Lu, A.Nathan, T.Manku and Y.Ning *Thin film magnetostrictive sensor with on-chip readout and attoFarad capacitance resolution* Technical Digest, IEEE IEDM 1996, pp. 777-780.

[10] A.Yariv and H.Winsor, *Proposal for Detection of Magnetic Fields Through Magnetostrictive Perturbation of Optical Fibers*, Opt.Lett. **5**, 87-89(1980)

[11] D.A.Jackson, A.Dandridge and S.K.Sheem, *Measurement of Small Phase Shifts Using a Single-Mode Optical Fiber Interferometer*, Opt.Lett.**5**, 139-141(1980)

[12] A.E.Clark, *Magnetostrictive Rare Earth-Fe_2 Compounds*, Ferromagnetic Materials, Vol.1, Edit by Wohlfarth (1980)

[13] Toshio Fukuda, Hidemi Hosokai, hiroaki Ohyama, Hideki Hashimoto and Fumihito Arai, *Giant Magnetostrictive Alloy (GMA) Application to Micro Mobile Robot as a Micro Actuator without Power supply cables*, Micro Electromechanical Systems 91 (MEMs91) 210-215

[14] P.M.Anderson III, *Magnetomechanical Coupling, ΔE Effect and Permeability in FeSiB and FeNiMoB Alloys*, J.Appl.Phys.**53**, 8101(1982)

[15] G.Y.Chin, *Processing Control of Magnetic Properties for Magnetostrictive Transducer Applications*, J.Metals, 42-25(1971)

[16] J.D.Livingston, *Magnetomechanical Properties of Amorphous Metal*, Physica Status Solidi A **70**, 591(1982)

[17] R.M.Bozorth, *Ferromagnetism*, (Van Nostrand, New York, 1953)p.628

[18] R.C.O'Handley, *Physics of Ferromagnetic Amorphous Alloys*, J. Appl. Phys. **62**, R15-R49 (1987)

[19] F.Bucholtz, K.P.Koo, A.M.Yurek, J.A.McVicker and A.Dandridge, *Preparation of Amorphous Metallic Glass Transducers for Use in Fibre Optic Magnetic Sensors*, J.Appl.Phys.**61**, 3790-3792(1987)

[20] F.Bucholtz, K.P.Koo, A.Dandridge and G.H.Sigel,Jr. *Easy Axis Distribution in Transversely Annealed Metglas 2605 S2*, J.Magn.Magn.Mat.**54-57**, 1607-1608(1986)

[21] J.Freestone, M.R.J.Gibbs and P.T.Squire, *Magnetoelastic Properties of sress-annealed Fe-Basee Metallic Glasses*, J.Appl.Phys.**70**, 6531-6533(1991)

[22] L.Kraus, N.Zarubova, K.Zaveta and P.Duhaj, *Creep-induced Magnetic Anisotropy of an Amorphous* $Fe_{80}Cr_2B_{14}Si_4$ *Alloy* J.Magn.Magn.Mater. **72**, 199 (1988).

[23] H.J.Oguey, *Sensitive Flux Measurement of Thin Magnetic Films*, The Review of scientific instruments **31**, 701 (1960)

[24] E.Klokholm, *The Measurement of Magnetostriction in Ferromagnetic Thin Films*, IEEE Trans.Magn.**MAG-12**, 819(1976)

[25] T.sato, H.Otake and Miyazaki, *Thickness Dependence of Magnetic Properties in an Amorphous* $Fe_{80.5}Si_{6.5}B_{12}C_1$ *Alloy* J.Magn.Magn.Mater. **71**, 263 (1988)

[26] E.M.Gyorgy, H.J.Leamy, R.C.Sherwood and H.S.Chen, AIP Conf.Proc. 29 (1975) 198

[27] F.Bucholtz, K.P.Koo, G.H.Sigel,Jr and A.Dandridge, *Optimization of the Fiber/Metallic Glass Bond in Fiber-Optic Magnetic Sensors* J.Lightwave Tech. **LT-3**, 814(1985)

[28] M.D.Mermelstein, *Amorphous Metal-Fiber Optic Magnetometer Response-Dipole Rotation Model*, J.Magn.Magn.Mater.**54-57**, 1473(1986)

[29] M.D.Mermelstein and A.Dandridge, *Low-frequency Magnetic Field Detection with a Magnetostrictive Amouphous Metal Ribbon*, Appl.Phys.Lett.**51**, 545(1987)

[30] A.Nathan and H.Baltes, *Integrated Silicon Magnetotransistors: High Sensitivity or High Resolution?*, Sensors and Actuators, **A21-23** (1990) 780-785

[31] L.I.Maissel, *The Deposition of Thin Films by cathode Sputtering*, Physics of thin Films, **3**, (1966) 61

[32] S.L.Rohde, *Unbalanced Magnetron Sputtering*, Physics of thin Films, **18**, (1994) 235

[33] F.Bucholtz *Fiber Optic Magnetic Sensors*, Fiber Optic Sensors, Edited by E.Udd, (1991) 367

[34] Properties of Silicon, IEE (1988) 654

[35] L.K.Baxter *Capacitive Sensors: Design and Applications* IEEE PRESS (1997)

[36] A.S.Sedra, K.C.Smith, Microelectronic Circuits, Saunders College Publishing (1991)

[37] T.Manku, IEEE Electron Device Letts., **17** (1996) 312

[38] P.Bergveld, *Development of an ion-sensitive solid-state device for neurophysiological measurements* IEEE Trans. Biomed. Eng. **19**, 70-71 (1970)

[39] K.E.Petersen, *Silicon as a Mechanical Material*, Proc.IEEE.**70**, 420(1982)

[40] J.H.Vleck, Rev.Mod.Phys.**17**, 27(1945)

[41] P.W.Anderson, *Magnetism*, Vol. I, Rado and Suhl eds., 25(1963)

[42] C.Kittel, *Physical Theory of Ferromagnetic Domains*, Rev.Mod.Phys.**21**, 541-580(1949)

[43] K.Honda, and S.Kaya, *On The Magnetization of Single Crystals of Iron*, Sci. Reports, Tohoku Univ, **15**, 721-753 (1926)

[44] S.Kaya, *On The Magnetization of Single Crystals of Nickel*, Sci. Reports, Tohoku Univ, **17**, 639-663 (1928)

[45] S.Kaya, *On The Magnetization of Single Crystals of Cobalt*, Sci. Reports, Tohoku Univ, **17**, 1157-1177 (1928)